

Alma Mater Studiorum Università di Bologna
Archivio istituzionale della ricerca

PD1 blockade potentiates the therapeutic efficacy of photothermally-activated and MRI-guided low temperature-sensitive magnetoliposomes

This is the final peer-reviewed author's accepted manuscript (postprint) of the following publication:

Published Version:

Guanglong Maa, Nina Kostevšekb, Ilaria Monaco, Amalia Ruiz, Boštjan Markelc, Calvin C.L. Cheung, et al. (2021). PD1 blockade potentiates the therapeutic efficacy of photothermally-activated and MRI-guided low temperature-sensitive magnetoliposomes. JOURNAL OF CONTROLLED RELEASE, 332, 419-433 [10.1016/j.jconrel.2021.03.002].

Availability:

This version is available at: <https://hdl.handle.net/11585/824068> since: 2021-06-21

Published:

DOI: <http://doi.org/10.1016/j.jconrel.2021.03.002>

Terms of use:

Some rights reserved. The terms and conditions for the reuse of this version of the manuscript are specified in the publishing policy. For all terms of use and more information see the publisher's website.

This item was downloaded from IRIS Università di Bologna (<https://cris.unibo.it/>).
When citing, please refer to the published version.

(Article begins on next page)

This is the final peer-reviewed accepted manuscript of:

Guanglong Ma, Nina Kostevšek, Ilaria Monaco, Amalia Ruiz, a Boštjan Markelc, Calvin C. L. Cheung, Samo Hudoklin, Mateja E. Kreft, Hatem A.F.M Hassan, Matthew Barker, Jamie Conyard, Christopher Hall, Stephen Meech, Andrew G. Mayes, Igor Serša, Maja Čemažar, Katarina Marković, Janez Ščančar, Mauro Comes Franchini, and Wafa T. Al-Jamal “PD1 blockade potentiates the therapeutic efficacy of photothermally-activated and MRI-guided low temperaturesensitive magnetoliposomes” Journal of Controlled Release 332 (2021) 419-433

The final published version is available online at:
<https://dx.doi.org/10.1016/j.jconrel.2021.03.002>

Terms of use:

Some rights reserved. The terms and conditions for the reuse of this version of the manuscript are specified in the publishing policy. For all terms of use and more information see the publisher's website.

This item was downloaded from IRIS Università di Bologna (<https://cris.unibo.it/>)

When citing, please refer to the published version.

PD1 blockade potentiates the therapeutic efficacy of photothermally-activated and MRI-guided low temperature-sensitive magnetoliposomes

Guanglong Ma,^{a†} Nina Kostevšek,^{b†} Ilaria Monaco,^c Amalia Ruiz,^a Boštjan Markelc,^d Calvin C. L. Cheung,^a Samo Hudoklin,^e Mateja E. Kreft,^e Hatem A.F.M Hassan,^a Matthew Barker,^a Jamie Conyard,^f Christopher Hall,^f Stephen Meech,^f Andrew G. Mayes,^f Igor Serša,^g Maja Čemažar,^d Katarina Marković,^h Janez Ščančar,^h Mauro Comes Franchini,^c and Wafa T. Al-Jamal^{a}*

† Both authors equally contributed to this manuscript

^a School of Pharmacy, Queen's University Belfast, Belfast, United Kingdom

^b Department for Nanostructured Materials, Jožef Stefan Institute, Ljubljana, Slovenia

^c Department of Industrial Chemistry "Toso Montanari", University of Bologna, Italy

^d Department of Experimental Oncology, Institute of Oncology Ljubljana, Ljubljana, Slovenia

^e University of Ljubljana, Faculty of Medicine, Institute of Cell Biology, Ljubljana, Slovenia

^f School of Chemistry, University of East Anglia, Norwich Research Park, Norwich, United Kingdom

^g Condensed Matter Physics Department, Jožef Stefan Institute, Ljubljana, Slovenia

^h Department for Environmental Sciences, Jožef Stefan Institute, Ljubljana, Slovenia

*Corresponding author:

Dr Wafa' T. Al-Jamal

School of Pharmacy

Queen's University Belfast

Belfast, BT9 7BL

United Kingdom

E-mail: w.al-jamal@qub.ac.uk

ABSTRACT

This study investigates the effect of PD1 blockade on the therapeutic efficacy of novel doxorubicin-loaded temperature-sensitive liposomes. Herein, we report photothermally-activated, low temperature-sensitive magnetoliposomes (mLTSL) for efficient drug delivery and magnetic resonance imaging (MRI). The mLTSL were prepared by embedding small nitrodopamine palmitate (NDPM)-coated iron oxide nanoparticles (IO NPs) in the lipid bilayer of low temperature-sensitive liposomes (LTSL), using lipid film hydration and extrusion. Doxorubicin (DOX)-loaded mLTSL were characterized using dynamic light scattering, differential scanning calorimetry, electron microscopy, spectrofluorimetry, and atomic absorption spectroscopy. Photothermal experiments using 808 laser irradiation were conducted. *In vitro* photothermal DOX release studies and cytotoxicity was assessed using flow cytometry and resazurin viability assay, respectively. *In vivo* DOX release and tumor accumulation of mLTSL(DOX) was assessed using fluorescence and MR imaging, respectively. Finally, the therapeutic efficacy of PD1 blockade in combination with photothermally-activated mLTSL(DOX) in CT26-tumor model was evaluated by monitoring tumor growth, cytokine release and immune cell infiltration in the tumor tissue. Interestingly, efficient photothermal heating was obtained by varying the IO NPs content and the laser power, where on-demand burst DOX release was achievable *in vitro* and *in vivo*. Moreover, our mLTSL exhibited promising MR imaging properties with high transverse r_2 relaxivity ($333 \text{ mM}^{-1} \text{ s}^{-1}$), resulting in superior MR imaging *in vivo*. Furthermore, mLTSL(DOX) therapeutic efficacy was potentiated in combination with anti-PD1 mAb, resulting in a significant reduction in CT26 tumor growth via immune cell activation. Our study highlights the potential of combining PD1 blockade with mLTSL(DOX), where the latter could facilitate chemo/photothermal therapy and MRI-guided drug delivery.

KEYWORDS: Anti-PD1, magnetoliposomes, iron oxide nanoparticles, photothermal, thermosensitive, theranostics.

Introduction

Mild localized hyperthermia (HT) (41 – 43 °C) has been used in combination with chemo and radiotherapy to enhance tissue perfusion, increase drug accumulation, and sensitize cancer cells to treatments [1]. HT has also been used as an external stimulus to trigger drug release from temperature-sensitive delivery systems, increasing drug bioavailability while reducing systemic toxicity [2]. ThermoDox[®] (Celsion Corporation) is the most developed low temperature-sensitive liposomes (LTSL) formulation. It is a liposomal formulation of doxorubicin (DOX), which undergoes a gel-to-liquid crystalline phase transition under mild HT (41 – 42 °C), resulting in an ultrafast drug release [3]. Celsion has completed a Phase 3 study of ThermoDox[®] with radiofrequency ablation (RFA) for the treatment of hepatocellular carcinoma (HCC), and there is currently an ongoing Phase 1 clinical trial (TARDOX study) for ThermoDox[®] in combination with high focused intensity ultrasound (HIFU) against liver cancer [4].

The suppressive tumor microenvironment is one of the main challenges faced in developing successful cancer therapies [5]. Recent studies have shown that mild HT upregulates the heat shock protein (HSP) indoleamine 2,3-dioxygenase and the cell death ligand 1 (PD-L1) on tumor cells, promoting self-protection and immunosuppression [6], which could counteract the therapeutic efficacy of existing thermal and photothermal therapy. Immune checkpoint inhibitors, such as anti-programmed cell death protein 1 (PD1) and anti-programmed cell death protein ligand 1 (PD-L1) monoclonal antibodies (anti-PD1 mAb), have shown promising results in cancer patients [7]. Similarly, DOX, an anticancer agent that induces immunogenic cell death (ICD)[8-12], has been found to upregulate PD-L1 on cancer cells [13]. PD1/blockade has been successful in improving the antitumor efficacy of DOX, DOXIL[®] and polymer-DOX nanoprodug in pre-clinical cancer models [14-16]. This collection of evidence highlights the importance of combinatory treatments simultaneously targeting cancer cells and their immunosuppressive microenvironment. Thus, it would be sensible to combine promising DOX-loaded thermoresponsive nanocarriers, with PD1/PD-L1 blockade to enhance their therapeutic efficacy *in vivo*.

To date, preclinical studies have triggered DOX release from LTSL using water bath HT [17] and high-focused ultrasound (HIFU)[18]. In the present work, we engineered multifunctional, photothermally-activated, low temperature-sensitive magnetoliposomes (mLTSL) for efficient DOX release and MRI. Furthermore, to tackle the immunosuppressive tumor microenvironment,

our photothermally-activated DOX-loaded mLTSL (mLTSL(DOX)) were co-administered with anti-PD1 mAb, emphasizing the importance of combining DOX-loaded thermosensitive liposomes with PD1/PD-L1 blockade for effective cancer therapy. Furthermore, the multifunctionality of our mLTSL could facilitate immuno/chemo/photothermal therapy and MRI-guided drug delivery.

Materials and Methods

Preparation of NDPM-coated iron oxide nanoparticles (IO NPs)

Hydrophobic nitrodopamine palmitate (NDPM)-coated iron oxide nanoparticles (IO NPs) and hydrophilic hydrocaffeic-acid (HCA) coated IO NPs were synthesized as we previously reported [19]. For the magnetic characterization, IO NPs were prepared in the form of a dry powder (10 mg). Magnetic measurements were performed with a vibrating-sample magnetometer (VSM MicroSense model FCM 10) at room temperature.

Preparation of low temperature-sensitive magneto-liposomes (mLTSL)

Dipalmitoylphosphatidylcholine (DPPC), and 1,2-distearoyl-*sn*-glycero-3-phosphoethanolamine-N-[methoxy(polyethylene glycol)-2000] (DSPE-PEG₂₀₀₀) were a kind gift from Lipoid, Germany. Monostearoylphosphatidylcholine (MSPC) was purchased from Avanti Polar Lipid, Alabaster, US. mLTSL were prepared using different lipid-to-NPs ratios. Briefly, 8.6 μ mol of DPPC (10 mg/mL), 1 μ mol of MSPC (5 mg/mL), 0.4 μ mol of DSPE-PEG₂₀₀₀ (10 mg/mL) and the different volumes of chloroform suspension of NDPM-coated IO NPs (0.1, 0.2, 0.3 or 0.5 mL) at a concentration 1 mg/mL were added to the lipid mixture, which results in the lipid-to-NPs ratio of 10, 20, 30 and 50 g/mol, respectively. The organic mixture was transferred to a round bottom flask (25 mL), and the lipid film was gradually dried using a rotary evaporator (Rotavapor R-100 equipped with heating bath, Interface I-100 and vacuum pump V-100, Bunchi, Switzerland) at 40°C. Once the lipid film was formed, the pressure in the flask was reduced to 33 mbar for 2 hours. The dried lipid film was then hydrated with 2 mL of 240 mM ammonium sulphate buffer ((NH₄)₂SO₄; pH 5.4) at 60 °C for 1 hour to achieve a final lipid concentration of 5 mM. Liposome size was reduced using the mini extruder (Avanti Polar lipid, USA). LTSL were prepared the same way, without adding NPs. Samples were extruded at 60 °C through 800 nm (5 cycles) and 200 nm (15 cycles) membrane filters (PC membranes, Avanti Polar lipid, USA). Empty LTSL and mLTSL

were left to anneal for 2 hours at room temperature then flushed with nitrogen and stored at 4°C for further experiments.

Preparation of DOX-loaded liposomes

DOX loading of empty LTSL and mLTSL was carried out using the pH-gradient method [20]. Briefly, liposomes were hydrated with 240 mM (NH₄)₂SO₄ buffer, pH 5.4. The desalting of liposomes suspensions was carried out using a PD10 column (GE Healthcare, UK) equilibrated with HBS (20 mM HEPES, 150 mM NaCl, pH 7.4). DOX-HCL (5 mg/mL, Apollo Scientific, BID0120) was added to the desalted liposomes suspensions at 1:20 DOX:lipid weight ratio. Subsequently, samples were incubated for 90 minutes at 37 °C. Free DOX was removed by gel filtration using a PD10 column, as described above. To quantify DOX, liposomes were lysed with 10% v/v Triton X-100 to achieve a final concentration of 1% v/v. Samples were transferred to a black-bottom 96-well plate (350 µL round wells, black polystyrene, Corning, USA), and fluorescence intensity of DOX was measured using an automated FLUOstar Omega (BMG Labtech, UK) plate reader ($\lambda_{\text{ex}} = 544 \text{ nm}$, $\lambda_{\text{em}} = 590 \text{ nm}$). DOX encapsulation efficiency (EE) was calculated by comparing the fluorescence intensity (I(t)) of DOX before and after purification (Eq. 1), diluted to the same final lipid concentration.

$$\text{Encapsulation efficiency (\%)} = \frac{I(t) \text{ after purification}}{I(t) \text{ before purification}} \times 100 \quad \text{Eq (1)}$$

Preparation of anti-PD1 functionalized LTSL

Maleimide functionalized LTSL (DPPC:MSPC:DSPE-PEG₂₀₀₀:Mal-DSPE-PEG₂₀₀₀; Mal-LTSL) (86:10:2:2 molar ratio) were prepared, the same way as described above. Next, 500 µg of anti-mouse PD1 (7.18 mg/mL; BE0146, Bio X Cell, USA), unless stated otherwise, were diluted in 400 µL of PBS-EDTA buffer (pH 8.0; 5 mM of EDTA) and 9.4 µL of Traut's reagent solution (2 mg/mL) were added to the prepared antibody solution under magnetic stirring for 3 minutes, and then incubated for 1 hour at 37° C. The thiolated antibody was then purified using a PD10 column and PBS-EDTA buffer, and mixed with prepared Mal-LTSL at a ratio of 50 µg of antibody to 1 µmol of lipid, and left stirring under N₂ overnight. The unconjugated anti-PD1 was removed using a qEV column (IZON SCIENCE LTD, qEVoriginal/70 nm). The conjugation efficiency was

determined using a Pierce™ BCA Protein Assay Kit, according to the manufacturer's recommendations.

Preparation of ICG-labeled liposomes

For *in vivo* imaging studies, ICG-labeled liposomes were prepared by mixing 20 µg of ICG (2 mg/mL in ethanol) with 8.6 µmol of DPPC (mg/mL), 1 µmol of MSPC (5 mg/mL), 0.4 µmol of DSPE-PEG₂₀₀₀ (mg/mL) to form the lipid film, and the liposomes were prepared, as described above.

Hydrodynamic diameter and zeta potential measurements

The hydrodynamic diameter, polydispersity index (PDI) and zeta potential of mLTSL with different lipid-to-NPs ratios were determined using Zetasizer Nano ZS90 (Malvern, UK) at 25°C. Disposable polystyrene cells and disposable plain folded capillary Zeta cells (Malvern, UK) were used. Suspensions were diluted in 0.2 µm filtered deionized water at ratios of 1:100 (v/v) for size measurements and 1:10 (v/v) for zeta-potential measurements.

Differential scanning calorimetry (DSC)

In order to determine the phase transition temperatures of the liposomes, 20 µL samples of LTSL and mLTSL at 10 mM concentration were placed in Tzero hermetic aluminum pans (TA Instruments) sealed with lids (Tzero hermetic lids, TA Instruments). DSC reference and sample cells were loaded with 20 µL of the reference buffer ((NH₄)₂SO₄, pH 5.4) and the liposome suspension, respectively. Samples were equilibrated at 30 °C for 2 minutes and then heated from 30 to 60°C at a heating rate of 1 °C min⁻¹ using a TA Q2000 Differential Scanning Calorimeter (TA Instruments) equipped with Universal Analysis software for data analysis.

Fourier-transform infrared spectroscopy (FTIR) measurements

FTIR measurements were performed in order to evaluate the success of the ligand binding to the NPs' surfaces. This was done by using a Spectrum 400 spectrometer (Perkin Elmer, USA). The spectra were recorded on dried samples in the wavenumber range 3500-900 cm⁻¹.

Atomic Absorption Spectroscopy (AAS)

Total concentrations of Fe of the analyzed samples were determined using Agilent 55 AA Atomic Absorption Spectrometer (Agilent Technologies, AU). A standard solution of Fe (1000 ppm \pm 1%/Certified, Fisher Chemical) was diluted with MilliQ water for the preparation of fresh calibration standard solutions. For the determination of Fe in aqueous suspension of mLTSL, 200 μ L of samples were dried using a block heater (Cole Parmer) at 100 °C, then 200 μ L of nitric acid (65 % HNO₃, Suprapur[®], VWR) were added and heated at 80 °C for 1 hour for acid digestion. After the digestion, the sample was diluted with MilliQ water to a final volume of 4 mL, and appropriately diluted prior to AAS measurements. Acid digestion was performed in triplicate. Fe content in each sample was determined using an Fe standard curve. For the tumor analysis the following procedure was applied. Each tumor sample was transferred to a Teflon beaker and 1.5 mL H₂O₂ (30 %, suprapure), 1 mL HNO₃ (65 %, suprapure) and 1.5 mL HCl (30 %, suprapure) were added. Sample was digested by microwave-assisted digestion (ramp to 140 °C for 15 minutes, hold 5 minutes, ramp to 180 °C for 15 minutes and hold 15 minutes). The digested sample was transferred to a 30 mL plastic tube and diluted with water to 30 mL. Further, an aliquot was diluted 10 times prior to ICP-MS analysis.

Transmission electron microscopy (TEM)

Samples for TEM analysis were prepared by adding a drop of NPs suspension on a holey carbon-coated TEM grid (300 mesh, AGS147-3, Agar Scientific, UK). Samples were prepared without staining. The morphology and size of the samples were analyzed using a transmission electron microscope (Jeol JEM-2100) operating at 200 kV for IO NPs and at 100 kV for liposomal samples.

Freeze fracture electron microscopy

For freeze-fracture electron microscopy, liposomes were initially cryoprotected by incubation in 30 % glycerol in 0.1 M cacodylate buffer for 60 minutes at 4 °C. Subsequently, 1.5 μ L of the sample was placed on the copper holder and fast-frozen by immersion into Freon, cooled by liquid nitrogen (-196 °C). Frozen samples were immediately transferred to freeze-fracture device (BALZERS, BAF200), fractured (knife temperature was -150 °C), shadowed with platinum (nominal angle 45°) and further strengthened by carbon (nominal angle 90°). Replicas were

transferred to room temperature and cleaned in a sodium hypochlorite solution. The cleaned replicas were picked on microscopic copper grids and were examined with a transmission electron microscope (Philips, CM100) running at 80 kV.

DOX release studies

Heat-inactivated fetal bovine serum (FBS) was purchased from Gibco (ThermoFisher Scientific). Laser triggered drug release studies were carried out by incubating the HBS buffer or FBS (0.25 mL) in a 37 °C water bath for 15 minutes and then transferred to an incubation chamber in order to stabilize the temperature. Next, DOX-loaded liposomes (0.25 mL) were added to the solution in each transparent cuvette. All samples were treated with an 808 nm laser at a power of 1.31 W/cm². At different time points, 0.05 mL of the sample were collected and diluted further with 0.15 mL of HEPES buffer. 0.1 mL of the samples above were transferred to a clear-bottom 96-well plate (350 µL round wells, black polystyrene, Corning, USA) and the fluorescence intensity was measured using a FLUOstar Omega (BMG Labtech, UK) plate reader. Based on the fact that DOX is quenched when it is loaded in the liposome, while it fluoresces more upon its release, the DOX-loaded liposomes without any treatment was used as a background control, and the difference between the samples and the background control reflected the percentage of the released DOX over time. Total DOX fluorescence was calculated following lysing liposomes with 0.02 mL of Triton X-100 solution (10 % v/v in HBS, pH 7.4).

Water bath triggered drug release studies were carried out by incubating the HBS buffer or FBS (0.25 mL) at 37 °C or 42 °C for 15 minutes, in order to stabilize the temperature. After that, DOX-loaded liposomes (0.25 mL) were added to the solution in each amber Eppendorf. At different time points, 0.05 mL of sample were collected and then followed the protocol described above. Measurements were performed in triplicate. The intensity of the fluorescence signals was then normalized and the percentage of DOX released was calculated using Eq. (2); where, I(s) is the fluorescence intensity of individual samples at any time point, I(0) is the background fluorescence intensity of DOX-liposomes, and I(t) is the total fluorescence intensity of Triton X-100 lysed liposomes.

$$\text{Release (\%)} = \frac{[I(s) - I(0)]}{[I(t) - I(0)]} \times 100\% \quad \text{Eq (2)}$$

Photothermal experiments

Photothermal experiments were performed using a FC-808 Fiber Coupled Laser System (CNI Optoelectronics Tech) configured for continuous wave operation at 808 nm with different power. The “incubation chamber” was made using a 3D printer MakerBot Replicator 2X. It was printed in ABS (acrylonitrile butadiene styrene) at 240 °C with a layer height of 0.1 mm. Additionally, we pumped 20 mL of acetone through the channels, waited for around 30 seconds and washed them with water to ensure watertight channels. A 3D model of the heating cell was made in SolidWorks 2014 and was prepared for printing in MakerBot Desktop 3.1. Outer dimensions of the 3D printed chamber: 3.7 x 3 x 3 cm. Inner hole for the cuvette: 1.3 x 1.3 cm. Window for the laser path: 1 x 1 cm. The incubation cell was connected to a water bath with tubes (diameter = 2 mm) and water heated to 41 °C was circulated using a peristaltic pump (Verderflex). Two tubes with a length of 25 cm were used to connect the peristaltic pump, the incubation cells and a water bath to a closed circuit. Under these conditions, the temperature inside the cuvette was maintained at 36 °C when the laser was turned off. Cuvette (size: 1 x 1 x 3 cm) containing 0.5 mL of a sample was irradiated with a laser beam through the opening in the incubation chamber. Laser light was focused on a cuvette using an optical lens at a fixed distance of 5 cm. The temperature of the suspension was measured with a fiber optic temperature probe (model PRB-G40, Osensa, Canada) that was immersed in the cuvette and connected to a computer (software Osensa View) to collect the data in real time. For Flow cytometry and cytotoxicity experiments, the well plates were sealed with parafilm and placed directly on the surface of 37 °C water bath to give a constant temperature at 36 °C. The laser light was focused on the treated well (other wells were covered to avoid crossed laser treatment) at a fixed distance of 5 cm with the desired power.

NMR relaxivity measurements

Hydrophilic hydrocaffeic acid (HCA)-coated IO NPs were synthesized as previously reported[19]. Iron content in the samples was determined using ICP-MS analysis. Aqueous suspensions of IO NPs and mLTSL were prepared in a concentration range (0.5 – 15 µg/mL = 0.009 – 0.27 mM) with respect to the Fe content. Relaxation time measurements of IO NPs and mLTSL were carried out using an NMR/MRI system consisting of a 2.35 T superconducting magnet (Oxford Instruments, Abingdon, UK), and an Apollo NMR spectrometer (TecMag,

Houston TX, USA). The T_1 relaxation times were measured using an inversion-recovery sequence with 14 different inversion times, ranging from 50 μ s to 10 s, while the T_2 relaxation times were measured using the Carr-Purcell-Meiboom-Gill (CPMG) sequence with multiple spin-echoes. The T_1 and T_2 relaxation times were calculated from the best fits between the measurements and the corresponding model for either T_2 relaxation (exponential dependency of the echo-signal on the echo number) or T_1 relaxation (dependency of the inversion recovery signal on the inversion time). The calculations were performed using the Origin program (OriginLab Corporation, Northampton MA, USA). The dependencies of the longitudinal ($1/T_1$) and transverse ($1/T_2$) relaxation rates on the Fe concentration in the sample were used to extract the relaxivities r_1 and r_2 . These are defined as proportionality constants between the contrast-agent-induced increase of the corresponding relaxation rate and the MRI contrast-agent concentration, as described by **Eq. (3)**.

$$R_1 = \frac{\left(\frac{1}{T_1}\right)_C - \left(\frac{1}{T_1}\right)_0}{C}, \quad R_2 = \frac{\left(\frac{1}{T_2}\right)_C - \left(\frac{1}{T_2}\right)_0}{C} \quad (3)$$

Here, C denotes the contrast-agent concentration, while the indexes C and 0 denote the relaxation rates at the contrast-agent concentration C and at zero concentration, respectively.

For T_2 -weighted MRI images the following conditions were used. The suspensions were arranged in a rosette-like stack, and then MRI scanned in the transverse orientation to the tubes multi-spin-echo sequences to obtain T_2 -weighted images. For imaging at 42 °C, samples were heated to 42 °C and inserted in the coil, where the constant temperature of 42 °C was maintained by the water circulating system and monitored using a fiber optic temperature probe. Geometrical and resolution parameters were the following: field of view 20 mm, imaging matrix 256 by 256 at 22 °C and 128 by 128 at 42 °C, no slice selection was used, while contrast parameters were TE/TR = 13/2000 ms (inter-echo time/repetition time) and number of echoes 8.

Cell culture

Murine colon (CT 26) cancer cells were obtained from American Type Culture Collection (ATCC, USA). Cells were cultured in Advanced RPMI 1640 (Invitrogen Gibco Life Technologies), supplemented with 10% FBS, 50 U/mL penicillin, 50 μ g/mL streptomycin, and 1% L-glutamine and maintained in a humidified chamber at 37° C and 5% CO₂ and passaged three times a week using 0.25% Trypsin-EDTA when reaching 80% confluence.

DOX release *in vitro*

CT26 cells (1×10^5 /well) were seeded overnight in 24-well plates. Then cells were incubated with 0.5 mL of LTSL(DOX) or mLTSL(DOX) ($[\text{Fe}] = 40 \mu\text{g/mL}$) at an equivalent DOX concentration of $2 \mu\text{M}$ and plates were sealed with parafilm. For cells treated with a laser (808 nm, 1.7 W/cm^2), their plates were placed directly on the surface of 37°C water bath. The laser light was focused on the treated well (the other wells were covered to avoid crossed laser treatment) at a fixed distance of 5 cm for 5 minutes. Then the plates were unsealed and put back into a humidified chamber at 37°C and 5% CO_2 for another 2 hours. For the cells treated with water bath, their plates were placed directly on the surface of a 42°C water bath for 1 hour, and the plates were unsealed and returned to a humidified incubator at 37°C and 5% CO_2 for another hour. Cells were washed 3 times using PBS and centrifuged (3000 rpm for 5 minutes). Then cells were resuspended in 600 μL of PBS and analyzed. For flow cytometry measurements, 10,000 cells in total were gated and the mean fluorescent intensity was determined.

Cytotoxicity studies

CT26 cells (1×10^4 /well) were seeded overnight in a 96 well-plate. Cells were incubated with 200 μL of mLTSL(DOX) ($\text{Fe} = 20 \mu\text{g/mL}$), LTSL(DOX), and free DOX at an equivalent DOX concentration of $1 \mu\text{M}$. For groups treated with a laser (808 nm, 1.7 W/cm^2), their plates were sealed with parafilm and placed directly on the surface of a 37°C water bath. The laser light was focused on the treated well (other wells were covered to avoid crossed laser treatment) at a fixed distance of 5 cm for 5 minutes. Then the plates were unsealed and put back into a humidified chamber at 37°C and 5% CO_2 for another 4 hours. Then cells were washed and replenished with fresh complete media and returned to the incubator at $37^\circ\text{C}/5\% \text{ CO}_2$ for another 20 or 44 hours. For groups that were not treated with the laser, their plates were kept in a humidified chamber all the time. Cell viability was assessed using resazurin assay. Briefly, cells were incubated with 0.01 mg/mL resazurin solution for 4 hours. After incubation, fluorescence ($\lambda_{\text{ex}} = 544 \text{ nm}$, $\lambda_{\text{em}} = 590 \text{ nm}$) was read using an automated FLUOstar Omega (BMG Labtech, UK) plate reader. Six replicates per condition were used. The results were expressed as the percentage of cell viability (mean \pm SD) and normalized to control untreated cells.

Binding capacity of anti-PD1-LTSL to CD8⁺ cells

For binding studies, fluorescently DiI-labeled LTSL and PD1-LTSL were prepared by incorporating 1 mol% DiI dye into the lipid film. To get the splenocytes, spleens were isolated from C57BL/6 mice, smashed through a 40 μ m cell strainer using the plunger from 1 mL syringe, followed by the treatment with ACK Lysis buffer (Thermo Fisher) to remove red blood cells. 0.5 million splenocytes were seeded in a 12-well plate, and incubated with DiI-labeled anti-PD1-LTSL or LTSL at a final lipid concentration of 0.25 (3 μ g/mL of anti-PD1 mAb) and 0.5 mM (6 μ g/mL of anti-PD1 mAb). 3 hours post-incubation, the cells were washed 3 times using PBS and centrifuged (3000 rpm for 5 minutes). To stain CD8⁺ T cells, the pellet was resuspended in 100 μ L of PBS, and 1 μ L of anti-Mo CD 8a (FITC, Clone 53-6.7, 0.5 mg/mL, Invitrogen) was added, and incubated at 4 °C for 30 minutes. Finally, cells were washed 3 times and resuspended in PBS. For flow cytometry measurements, 50,000 cells in total were gated as R1. Then, in R1, stained CD8⁺ T cells population with a fluorescent intensity higher than 1×10^2 were gated as R2. Next, DiI-labeled cells populations with a fluorescent intensity higher than 30 from R2 were gated as R3. The population ratio between R3/R2 was used to calculate the ratio of PD1⁺CD8⁺/CD8⁺ T cells.

Animals and tumor model

5-week-old female BALB/c mice were purchased from Envigo (Bicester, UK) and animal procedures were performed in compliance with the UK Home Office Code of Practice for the Housing and Care of Animals used in Scientific Procedures. Mice were inoculated with 2.5×10^5 CT26 cancer cells in 20 μ L PBS by subcutaneous injection in the right lower leg using 27 G hypodermic needles.

***In vivo* Imaging**

Mice with suitable tumor size were placed on Teklad Global 2019X food Envigo (Bicester, UK) 5 days prior to imaging, and shaved using a hair removal cream. **To ensure that injected DOX was detectable *in vivo*,** tumor-bearing mice (n=3) were injected *via* the tail vein with equivalent doses of 8 mg/kg of DOX & 0.5 mg/kg of ICG (in 200 μ L HBS) of LTSL(DOX)-ICG, mLTSL(DOX)-ICG (60 μ g of Fe), and mLTSL(DOX)-ICG+anti-PD1-LTSL-ICG (60 μ g of Fe & 50 μ g of anti-PD1 mAb). All groups were injected the same dose of DOX, ICG and lipid. After injection, mice were anesthetized with isoflurane, and one magnet disc (8 mm, Magnet Expert,

F645-N52-10) was taped to one tumor-bearing leg for 50 minutes, and followed by laser exposure (0.3 W/cm^2) for 10 minutes to avoid non-specific heating. The tumor sites' temperature was monitored with FLIR C3 thermal camera (FLIR Systems UK, Kent, UK). The mice body temperature was monitored using a heating pad and a rectal thermocouple. Immediately, after the irradiation, mice were imaged using the Bruker InVivo Xtreme imaging system with an exposure time of 10 s, for ICG ($\lambda_{\text{ex}} = 760 \text{ nm}$, $\lambda_{\text{em}} = 830 \text{ nm}$) and DOX ($\lambda_{\text{ex}} = 480 \text{ nm}$, $\lambda_{\text{em}} = 600 \text{ nm}$), respectively. Then mice were re-imaged 24 hours post-injection. At the end of the study, mice were sacrificed, and the organs and tumors were collected and imaged, as described above. Images were analyzed with Molecular Imaging software. For quantification, Region of Interest (ROI) analysis was applied.

Magnetic resonance imaging (MRI) procedures were performed in compliance with the guidelines for animal experiments of the EU Directives, ARRIVE Guidelines and the permission of the Ministry of Agriculture Forestry and Food of the Republic of Slovenia (Permission No. U34401-1/2015/43). Tumor-bearing mice ($n=3$) were injected *via* the tail vein with HCA-IO NPs or MLs with total Fe concentration of $50 \mu\text{g}$. After injection, mice were anesthetized with isoflurane, and one magnet disc (8 mm, Magnet Expert, F645-N52-10) was taped to one tumor-bearing leg for 50 minutes, and followed by laser exposure (0.3 W/cm^2) for 10 minutes. The tumor sites' temperature was monitored with FLIR C3 thermal camera (FLIR Systems UK, Kent, UK). Immediately, after the irradiation, magnet was removed and mice were imaged using 2.35 T NRM/MRI scanner, i.e. imaging 1 hour post-injection. T_1 - and T_2 -weighted images were recorded using the following sequences: $\text{TE/TR} = 5/400 \text{ ms}$ and $\text{TE/TR} = 40/3000 \text{ ms}$, respectively. Then mice were re-imaged 24 hours post-injection. For each mouse, 9 slices (2 mm) with a field of view of 30 mm for both imaging modalities were recorded in a transverse plane to cover the entire tumor region. Slice 5 that represents the best the core of both tumors and was thus selected for the comparison purposes.

Therapy experiment

Mice with tumor size around $50 - 100 \text{ mm}^3$ were grouped randomly. Each group ($n=5$) was injected *via* the tail vein with PBS ($200 \mu\text{L}$), free DOX (2 mg/kg), mLTSL(DOX) (DOX: 2 mg/kg , Fe: 3 mg/kg), mLTSL(DOX)+anti-PD1-LTSL (DOX: 2 mg/kg , Fe: 3 mg/kg , PD1 mAb: 2.5 mg/kg), LTSL(DOX) (DOX: 2 mg/kg), anti-PD1-LTSL(DOX) (DOX: 2 mg/kg , anti-PD1: 2.5

mg/kg), and anti-PD1 mAb (2.5 mg/kg). Following the injection, mice were anaesthetized, and one magnet disc was taped to the tumor-bearing leg for 50 minutes, and followed by laser exposure (0.3 W/cm^2) for 10 minutes to trigger drug release. The body temperature was monitored using a heating pad and a rectal thermocouple. The dose was repeated twice on day 12 and 15 post-inoculation. Tumor growth was monitored three times a week using an electronic caliper, and tumor volume was calculated using $V=L*W^2/2$ (V: tumor volume, L: the longest diameter, W: the diameter perpendicular to the length). Body weight was monitored three times a week, and mice were terminated at endpoint.

Immune response study

Tumor-bearing mice were treated as described in the therapy experiment. 17 days post-tumor inoculation, mice were sacrificed, and blood and tumors were collected. Blood was kept in the fridge overnight, then centrifuged at 2000 rpm for 5 minutes, and the serum was collected and used for IFN- γ test, following the manufacturer's protocol (IFN gamma Mouse Uncoated ELISA Kit, Invitrogen).

Tumor cells were collected by smashing the tumors through a 70 μm cell strainer. Isolated tumor cells were then washed with cold PBS twice. The cells were resuspended in 100 μL of PBS (containing 2% FBS), and individually stained with 1 μL of anti-Mo CD8a-FITC (0.5 mg/mL, Invitrogen) or CD4-FITC (0.5 mg/mL Invitrogen) for 20 minutes at 4 $^{\circ}\text{C}$ in the dark. Then, cells were washed twice with cold PBS and resuspended in 600 μL PBS for flow cytometry analysis. Briefly, 10,000 cells in total were counted, and gated as R1. Then, stained CD8 $^{+}$ T cells population with a fluorescent intensity higher than 1×10^2 were gated as R2. The population ratio of R2/R1 was defined as % CD8 $^{+}$ T cells/tumor. The same was applied to CD4 $^{+}$ T cells analysis.

Statistical analysis

One-way ANOVA or unpaired two-tail Student's t-test was used for our statistical analysis. The specific test used is described in the figure captions. The data were presented as mean \pm SD for all experiments except for *in vivo* studies, where the data were presented as mean \pm SEM (n represents the number of repeats). Differences were considered significant at $p < 0.05$, * $p < 0.05$, ** $p < 0.01$, *** $p < 0.001$, **** $p < 0.0001$. Statistical analysis was performed with GraphPad Prism 7.0 (GraphPad Software, Inc., San Diego, CA).

Results

Preparation of stable mLTSL by embedding hydrophobic IO NPs into LTSL lipid bilayer.

Small oleic acid-coated iron oxide nanoparticles (IO NPs) were synthesized with a diameter of 4.5 ± 1 nm, as confirmed by the transmission electron microscopy (TEM) analysis (**Figure S1A**). According to the selected area diffraction pattern (SAED) analysis and its comparison to the calculated diffraction pattern (ICSD 65340), IO NPs had a cubic inverse spinel crystal structure (**Figure S1B**). The magnetic measurement of the OA-coated IO NPs (**Figure S1C**) confirmed the superparamagnetic nature of NPs with a saturation magnetization of 32 emu/g, which is a typical value for Fe₂O₃ NPs of 4 nm nanoparticles [21]. The OA surface ligand was then replaced with the nitrodopamine palmitate (NDPM) ligand to enhance NPs incorporation into the lipid bilayer [22]. Fourier-transform infrared (FTIR) spectroscopy was used to confirm the successful ligand-exchange reaction. FTIR spectra of the soluble NDPM ligand, OA-coated IO NPs and NDPM-coated IO NPs are shown in **Figure S1D**. The characteristic band at 1705 cm⁻¹ for the C=O stretch of the hydrogen-bonded OA was not present in the FTIR spectrum for NDPM-coated IO NPs, which indicates complete ligand exchange [19]. Moreover, characteristic bands for the pure NDPM ligand can be found in the spectrum for NDPM-coated IO NPs, which therefore indicates the presence of the NDPM ligand on the surface IO NPs (consult Supporting Information for the detailed description of these bands).

Scheme 1

Magneto-LTSL (mLTSL) were prepared by incorporating the small NDPM-coated IO NPs in the LTSL lipid bilayer at different NPs-to-lipid ratios (**Scheme 1**). mLTSL were characterized using dynamic light scattering (DLS) to determine their hydrodynamic size and surface charge (**Table 1**). The slightly increased the mLTSL's hydrodynamic diameter (138-157 nm) compared to the empty LTSL (121 nm) could be an evidence that small NDPM-coated IO NPs (4.5 nm) were loaded into the lipid bilayer. A slight increase in the polydispersity index (PDI) was also observed (from 0.07 to 0.11). Zeta potential measurements (**Table 1**) indicated no significant changes in the liposomes' surface charge following IO NPs encapsulation. Over time, no IO NPs aggregation or precipitation was observed, indicating good colloidal stability.

Table 1

Next, mLTSL loaded at different NPs-to-lipid ratios was examined under the TEM (**Figure 1**). It is worth mentioning that unstained liposomes were used to visualize the small, electron-dense IO NPs in the samples; therefore, the liposomes' lipid bilayers were not visible. It was evident that more IO NPs were detected in the mLTSL formulated with higher IO NPs (**Figure 1A-C**). To quantify the IO NPs incorporated into liposomes, Fe content in the prepared mLTSL was determined using atomic absorption spectroscopy (AAS), as shown in **Table 1**. By increasing the NPs-to-lipid ratios (10 – 50 g/mol) the Fe content in the mLTSL increased from 1.8 to 7.3 g/mol. This result was in agreement with the TEM images (**Figure 1A-C**), where a higher amount of NPs was observed. **Table 1** shows no significant differences in the phase transition temperatures between all formulations (T_c is 42.5 °C and 42.3 °C for LTSL and mLTSL, respectively), indicating that the presence of IO NPs did not adversely affect the lipid bilayer. Furthermore, our results show that the mLTSL exhibited high DOX loading efficiency (> 90%), suggesting that the presence of the IO NPs in the lipid bilayer did not affect DOX loading (**Table 1**), except for the highest NPs-to-lipid ratio (~EE = 78 %).

Figure 1

To elucidate the structure of the mLTSL(DOX), freeze-fracture electron microscopy (FF-EM) was used. Interestingly, FF-EM images revealed a change in the LTSL morphology following DOX-loading, where elongated vesicles (indicated by the yellow arrows) were present, compared to the empty spherical LTSL (**Figure 1D&E**); however, no DOX crystals were observed. On the other hand, our mLTSL(DOX) exhibited a highly punctuated surface and elongated vesicles, indicating the co-loading of IO NPs and DOX in the liposome bilayer and aqueous core, respectively (**Figure 1F**).

Finally, the colloidal stability of the mLTSL's dispersions and their ability to be magnetically manipulated were evaluated by exposing the mLTSL to an external magnetic field. As expected, the mLTSL were attracted to the magnet and the mLTSL pellet was easily re-dispersed (**Figure 1G**) without affecting the colloidal properties (size and PDI) of the mLTSL (**Figure 1H**).

mLTSL as a promising MRI T_2 contrast agent

The effectiveness of our mLTSL as an MRI contrast agent was investigated by measuring the dependence of the longitudinal (T_1) and transverse (T_2) relaxation times on the Fe concentration ($0.5 - 15 \mu\text{g/mL} = 0.009 - 0.27 \text{ mM}$) in the samples (**Figure S2a** and **S2b**). The values were then used to calculate longitudinal (r_1) and transversal relaxivities (r_2) which are listed in **Table 2** & **Figure S2c** and **S2d**. In order for the material to be an effective T_2 agent, a high r_2 value is a prerequisite, with the r_2/r_1 ratio equal to 10 or more [23].

Table 2

For this study, an aqueous suspension of hydrophilic hydrocaffeic acid (HCA)-coated IO NPs was prepared *via* a ligand exchange reaction [19] and used for comparison. This approach offers hydrophilic IO NPs with the same core of NDPM-coated IO NPs that were used for mLTSL preparation. The highly negative zeta potential measurement ($-42 \pm 1.1 \text{ mV}$ at pH 7) confirmed the successful ligand-exchange reaction the (HCA)-coated IO NPs, which is related to the deprotonation of the carboxylic group of the HCA ligand [24]. High measured values of the zeta-potential enable a strong electrostatic repulsion between the NPs, which results in persistent suspension stability for a period of several months. The relaxivity values for HCA-coated IO NPs were $r_1 = 0.85 \pm 0.04 \text{ mM}^{-1} \text{ s}^{-1}$ and $r_2 = 3.2 \pm 0.8 \text{ mM}^{-1} \text{ s}^{-1}$. These results showed that the IO NPs have a weaker effect on the shortening of the T_1 than the T_2 relaxation times, which is an expected behavior due to the superparamagnetic nature of the IO NPs, which are usually classified as T_2 contrast agents [25]. In comparison, r_2 value was significantly increased ($r_2 = 333 \pm 13 \text{ mM}^{-1} \text{ s}^{-1}$) and r_1 was lowered from $0.85 \text{ mM}^{-1} \text{ s}^{-1}$ to $0.29 \text{ mM}^{-1} \text{ s}^{-1}$ when IO NPs were embedded into LTSL bilayer. As a result of the simultaneous decrease of r_1 and increase of r_2 values, mLTSL with $r_2/r_1 = 1148$ are much more efficient T_2 MRI contrast agents than the “free” HCA-coated IO NPs ($r_2/r_1 = 3.8$), which could suggest our mLTSL as a promising MRI contrast agent. Due to the thermosensitive nature of our liposomal formulation, T_2 weighted MRI images were recorded at 22°C and 42°C (**Figure S3**). As expected, mLTSL provided significantly better contrast (darker image) than HCA-coated IO NPs. The increase in temperature did not affect the contrast capability of mLTSL, probably due to the incorporation of the IO NPs in the lipid bilayer, rather than the liposomal aqueous core.

808 nm laser efficiently heats mLTSL inducing ultrafast DOX release and selective cytotoxicity *in vitro*.

The photothermal heating capacity of mLTSL with different concentrations of Fe was tested using an 808 nm laser with a power of 0.55 – 1.7 W/cm² (**Figure 2A-D**). As expected, high Fe concentrations and/or high laser power led to a higher temperature increase after 10 minutes of irradiation. Importantly, at low laser power (0.55 W/cm²), samples containing more than 32 µg/mL of Fe reached the desired mild HT temperature (< 45 °C). Upon increasing the laser power, a higher increase in temperature was achieved using lower Fe concentrations; however, high laser power resulted in undesirable heating (~39 °C) of the control sample (HBS buffer only). These findings indicate that our mLTSL can be used as a safe and efficient drug delivery system, where fast drug release can be remotely triggered using a low-intensity NIR laser in combination with relatively low concentrations of IO NPs. Nevertheless, photothermal ablation can also be obtained by tuning the laser power and the Fe content in the mLTSL.

Figure 2

To determine whether laser-induced HT is capable of triggering burst drug release, LTSL(DOX) and mLTSL(DOX) with an intermediate Fe concentration (i.e. [Fe] = 20 µg/mL), were irradiated with an 808 nm laser (1.31 W/cm²). Water bath-induced HT was used as a control. DOX release profiles were determined in HBS pH 7.4 or 50% serum at 42 °C. **In contrast to LTSL(DOX) without IO NPs, all mLTSL(DOX) samples (HBS & 50% FBS) released 100% of DOX after 5 minutes of irradiation (Figure 2E).** This clearly shows that the presence of IO NPs is crucial for achieving selective heating and, consequently, burst drug release. **The DOX release profile of laser-irradiated mLTSL was comparable to incubating LTSL(DOX) and mLTSL(DOX) in a 42 °C water bath (Figure 2F).** It is worth mentioning that both LTSL(DOX) and mLTSL(DOX) exhibited comparable stability at 37 °C in HBS and 50% FBS (**Figure S4**). These findings agree with the DSC results and prove that embedding small IO NPs into the LTSL lipid bilayer does not adversely affect LTSL stability and thermoresponsiveness.

Next, the biological activity of the mLTSL(DOX) in cells was assessed. In these experiments, CT26 cells were seeded in 24-well plates for 24 hours. The cells were then incubated with LTSL(DOX) or mLTSL(DOX) at a final DOX concentration of 2 µM. One group was irradiated with the laser (1.7 W/cm², **Figure 2G, left**) for 5 minutes and returned to the incubator

(37 °C, 5% CO₂) for 1 hour and 55 minutes. The second group was incubated for 1 hour at 42 °C using a water bath (**Figure 2G, right**) and returned to the incubator for another hour. Flow cytometry was used to study DOX cell uptake by comparing the change in mean fluorescence intensity of laser or water bath treated cells vs. non-heated cells (i.e. 37 °C). As expected, cells incubated with mLTSL(DOX) following the laser irradiation resulted in about a 3-fold increase in DOX fluorescence, due to the laser-induced HT DOX release. In contrast, no fluorescence change was observed for the laser-irradiated LTSL(DOX) samples (**Figure 2G**). To confirm the higher cell uptake caused by DOX release from the liposomes, a 42 °C water bath was used to trigger DOX release from both LTSL(DOX) and mLTSL(DOX). **Figure 2G** shows that cells incubated with both formulations exhibited a 3.5-fold increase in DOX fluorescence intensity, compared to unheated cells.

Finally, *in vitro* cytotoxicity of mLTSL(DOX) was evaluated in CT26 cells. First of all, no significant decrease in the cell viability was observed in cells incubated for up to 72 hours with mLTSL containing different concentrations of Fe (0.01 – 20 µg/mL), indicating the high biocompatibility of our mLTSL (**Figure S5A**). As expected, laser irradiation with different laser power (0.5 – 1.7 W/cm²) did not induce any toxicity (**Figure S5B**), proving that the laser light under these conditions was harmless to the cells. Furthermore, CT26 cells incubated with mLTSL (20 µg/mL of Fe) and irradiated with the laser (1.7 W/cm² for 5 minutes) did not induce any reduction in cell viability for up to 24 hours after treatment (**Figure S5B**, Fe+L column). All these findings suggest that our observed toxicity is primarily due to DOX release from mLTSL. To test our hypothesis, cells were incubated with free DOX, LTSL(DOX) or mLTSL(DOX) at a final concentration of 1 µM DOX, and cell viability was assessed in the presence (+L) and absence (-L) of the laser (1.7 W/cm² for 5 minutes). 4 hours post-irradiation, cells were washed, and wells were replenished with complete fresh media. Cell viability was assessed after 24 and 48 hours (**Figure 2H**) using resazurin assay. At the 24-hour time-point, cells incubated with free DOX or LTSL(DOX) showed similar cell viability (approx. 60%) regardless of laser irradiation. On the other hand, lower cell viability (40%) was detected in the cells treated with mLTSL(DOX) and irradiation (+L), compared with the non-irradiated (-L) cells (65%). 48 hours after treatment, the viability of cells treated with free DOX (+L & -L) remained about 60%. However, the viability of the cells incubated with LTSL(DOX) (-L and +L) and mLTSL(DOX) (-L) significantly increased to 80%, indicating cell recovery due to incomplete DOX release. Interestingly, the viability of cells

treated with mLTSL(DOX) and laser (+L) remained below 50%, indicating irreversible cell damage caused by a high concentration of bioavailable DOX.

Anti-PD1-functionalized LTSL (anti-PD1-LTSL) binding CD8⁺ T cells *in vitro*.

To enable PD1 targeting to activated T cells, anti-mouse PD1 monoclonal antibodies (anti-PD1 mAb) were conjugated to low temperature-sensitive liposomes (LTSL), as described in **Figure 3A**. Anti-PD1 mAb was first thiolated by Traut's reagent, then conjugated to LTSL containing different amounts of maleimide-functionalized lipid. Successful anti-PD1 mAb conjugation was achieved with an efficiency ranging between 16 – 27.5 g/mol lipid, with slight changes in LTSL size (**Table S1**). Anti-PD1-LTSL with a conjugation efficiency of 16 g/mol were selected for our *in vitro* studies. These anti-PD1-LTSL exhibited smaller hydrodynamic size (156.9 ± 5.4 nm) and lower PDI (0.17 ± 0.1) after functionalization (**Table S1**), which is still suitable for intravenous administration [26].

Figure 3

Next, the binding capacity of anti-PD1-LTSL to CD8⁺ T cells was determined. Isolated splenocytes were incubated for 3 hours with fluorescently DiI-labeled, anti-PD1-LTSL (3 μ g PD1 mAb/0.25 μ mol lipid or 6 μ g PD1 mAb/0.5 μ mol lipid) or equivalent non-targeted LTSL. The splenocytes were washed and CD8⁺ T cells were stained with FITC-labeled anti-Mo CD8a mAb. The binding capacity of anti-PD1-LTSL to CD8⁺ cell population was studied using flow cytometry and the percentage ratio of PD1⁺ CD8⁺ to whole CD8⁺ cells was calculated. **Figure 3B** shows that anti-PD1-LTSL exhibited consistently higher binding to CD8⁺ T cells compared to the non-targeted LTSL, indicating that PD1 targeting was preserved following LTSL conjugation.

Laser-induces DOX release from mLTSL *in vivo*.

In vivo fluorescence imaging was used to investigate the biodistribution of mLTSL(DOX) and its DOX release behavior in CT26 tumor-bearing mice. All liposomal formulations, namely LTSL(DOX)-ICG, mLTSL(DOX)-ICG, and mLTSL(DOX)-ICG+anti-PD1-LTSL-ICG, where the lipid bilayers were labeled with an equivalent concentration of the FDA-approved indocyanine green (ICG) to track their *in vivo* biodistribution [27, 28], and loaded with equivalent DOX to test their DOX releasing in response to laser irradiation. Preparation of anti-PD1-mLTSL(DOX),

which was the main intention of this project, was not possible to engineer due to severe aggregation of the mLTSL during the anti-PD1 mAb conjugation step in the presence of a magnetic stirrer (data not shown). Bubbling the reaction mixture under nitrogen was attempted but undesirable results were obtained (data not shown); therefore, mLTSL(DOX) were mixed with anti-PD1-LTSL and administered in a single dose. Since our results showed that the magnet could attract the mLTSL without affecting their colloidal properties (**Figure 1H**), mice were intravenously injected with different formulations. Then one tumor-bearing leg was immediately taped with one magnet disc for 50 minutes to enhance mLTSL accumulation at the tumor site. The tumor was then irradiated with the laser (808 nm, 0.3 W/cm²) for 10 minutes (labeled as +L) to minimize non-specific heating of the tumor. The tumor on the second leg was not exposed to the magnet nor to laser irradiation, and was labeled as (-M,-L). Live fluorescence imaging was carried out at 70 minutes and 24 hours post-injection to monitor DOX release (**Figure 4A**) and ICG-labeled liposomes tumor accumulation (**Figure 4B**).

Figure 4

DOX-based fluorescence images (**Figure 4A & 4C**) of the mice treated with LTSL(DOX)-ICG, taken 70 minutes and 24 hours after injection, showed weak DOX fluorescence signals at both tumor sites (+M,+L and -M,-L). In contrast, both mLTSL(DOX)-ICG and mLTSL(DOX)-ICG+anti-PD1-LTSL-ICG in combination with laser treatment (+M, +L) showed higher DOX release at the tumor site, while non-irradiated tumors (-M, -L) showed no obvious evidence of DOX release, indicating a fast, efficient and remote release from the mLTSL *in vivo*, using a low-power 808 nm laser. 24 hours after injection, DOX signals slightly increased in the tumors of the mice treated with LTSL(DOX)-ICG, which means that DOX-loaded liposomes could passively accumulate in the tumor site based on the enhanced permeation and retention (EPR) effect. In the mLTSL group, the DOX signals in tumor (+M,+L) decreased compared to 70 minutes post-injection due to free DOX metabolism or washout [17]. Interestingly, *ex vivo* examination revealed consistently higher DOX fluorescence in mice injected with LTSL (+M,+L & -M,-L) and mLTSL (-M,-L) (**Figure S6**). This could be attributed to the hypothesis that encapsulated DOX slowly accumulated and washed out from tumor tissues [17].

Liposome biodistribution was also determined by tracking ICG fluorescence in mice. After 70 minutes post-injection, mice treated with LTSL(DOX)-ICG, showed no obvious ICG

fluorescence difference between +M,+L and -M,-L. On the other hand, mice injected with mLTSL(DOX)-ICG and mLTSL(DOX)-ICG+anti-PD1-LTSL-ICG, showed higher ICG signals in the irradiated tumors, compared to non-irradiated tumors and LTSL(DOX)-ICG group (**Figure 4B & 4C**). This could be attributed to laser induced-hyperthermia (43-44 °C) (**Figure 4D**), which increased the blood flow to the tumor site [29, 30] and triggered DOX release, which works as a vascular damaging agent (**Figure 4E**) [31]. 24 hours post-injection, detectable ICG signals were observed in all injected groups, which indicates passive accumulation of these ICG-labeled liposomes. Despite the obvious reduction in ICG signals 24 hours post-irradiation, higher ICG signals were still present in mice injected with mLTSL(DOX)-ICG and mLTSL(DOX)-ICG+anti-PD1-LTSL-ICG, as confirmed *in vivo* (**Figure 4B**) and *ex vivo* (**Figure S6**).

mLTSL as efficient *T2* contrast agents *in vivo*

MRI was used to monitor the accumulation of HCA-IO NPs and mLTSLs in the tumors. Comparison of *T1*- and *T2*-weighted images (**Figure S7**) clearly show that *T2*-weighted images can distinguish between normal muscle (darker tissue, M) and brighter tumor tissue (T). In contrast, in *T1*-weighted images, both tissues have the same contrast. Therefore, *T2* images are better to observe pathological changes and *T1* images to see anatomy.

Figure 5

In all animal groups, following injection, one tumor was exposed to the magnet then irradiated with a laser (+M, +L) while the second tumor was used as a control (-M, -L). **Figure 5A** represents the *T2*-weighted images HCA-IO NPs- and mLTSL-injected mice. As expected, 1 hour following the intravenous injection of the HCA-IO NPs, some darker areas were only visible in the centre of the tumor exposed to the magnet (+M +L, yellow arrows) with some reduced signal contrast after 24 hours. In the non-treated tumor (-M,-L) no changes in the contrast could be observed (green arrows). Moreover, no changes in the contrast were evident on *T1* image (**Figure S7**), confirming IO NPs as *T2* and not *T1* contrast agents. Importantly, injection of mLTSL with the same Fe content led to a significant darkening of the tumor site on *T2* image (+M,+L, red arrows, **Figure 5A**) compared to the HCA-IO NPs, indicating their superiority as a *T2*-contrast agent. More interestingly, stronger contrast signals were detected 24 hours in both tumors (+M,+L red arrows & -M,-L green arrows) injected with the mLTSL, suggesting passive tumor targeting. The latter

finding is in good agreement with the *in vivo* imaging (**Figure 4B**), indicating prolonged mLTSL blood circulation combined with good *in vivo* stability. To quantitatively evaluate the accumulation of mLTSL and HCA-IO NPs in the tumors, Fe content in tumors was determined using ICP-MS analysis (**Figure 5B**). Mice were sacrificed at the end of the study, and tumors were collected. High levels of Fe was detected in tumors injected with mLTSL and HCA-IO NPs (+M,+L) compared to HCA-IO NPs (-M,-L), which is in agreement with the MRI images. Interestingly, this finding confirms the superiority of the mLTSL as a *T2* contrast agent to HCA-IO NPs at an equivalent Fe level.

Combining PD1/PD-L1 blockade with photothermally-triggered mLTSL(DOX) significantly delays tumor growth *in vivo*

To assess the effectiveness of combining PD1/PD-L1 blockade with photothermally-triggered mLTSL(DOX), CT26-tumor-bearing mice were injected *via* their tail vein on day 12 and day 15 post-tumor inoculation with intravenously injected PBS (Group 1), free DOX (Group 2), anti-PD1 mAb (Group 3), mLTSL(DOX) (Group 4), mLTSL (DOX)+anti-PD1-LTSL (Group 5), LTSL (DOX) (Group 6), and LTSL (DOX)+anti-PD1-LTSL (Group 7). All tumors were irradiated with the laser (0.3 W/cm² for 10 minutes). The antitumor efficacy was assessed by measuring tumor volume over time. **Figure 6A** shows that PBS-treated mice showed the fastest tumor growth, whilst mLTSL(DOX)+anti-PD1-LTSL was the most effective treatment in delaying tumor growth. Treatment with free DOX (Group 2), free anti-PD1 mAb (Group 3), mLTSL(DOX) (Group 4), LTSL (DOX) (Group 6), and LTSL (DOX)+anti-PD1-LTSL (Group 7) in combination with laser irradiation moderately inhibited tumor growth with no significant differences between the groups (**Figure 6A**). Unexpectedly, mLTSL(DOX)+laser (Group 4) showed similar tumor inhibition compared to LTSL(DOX)+laser (Group 6), which could be due to the low DOX dose (2 mg/kg) administered during the whole treatment, where more frequent injections of mLTSL(DOX) or higher DOX doses could have resulted in more significant tumor inhibition compared to LTSL(DOX)+laser. During the whole experiment, no obvious bodyweight drop was observed (**Figure S8**).

Figure 6

Following the tumor growth delay study, we investigated if the combined treatment was associated with immune cell activation *in vivo*. For this study, tumor-bearing mice received the same treatments described above (Group 1 – 5), then serum and tumor CD4⁺ and CD8⁺ T cells were isolated 72 hours after the second dosage. In agreement with our growth delay results, the combined treatment (Group 5) showed the highest serum IFN- γ level (>100 pg/mL), indicating successful systemic response activation (**Figure 6B**). Mice injected with mLTSL(DOX) (Group 4) showed a IFN- γ level around 55 pg/mL, which is also a significant increase compared to PBS- or free DOX-injected groups (Group 1 & 2, respectively) (none detectable by the ELISA kit, which has an analytical sensitivity over 16 pg/mL), indicating that mLTSL(DOX) alone could trigger a systemic immune response. Furthermore, mice injected with anti-PD1 mAb (Group 3) exhibited a slight but significant increase in serum IFN- γ (~20 pg/mL) compared to PBS-treated mice (Group 1). A similar trend was observed in tumor CD4⁺ and CD8⁺ T cell analysis. The combination of mLTSL(DOX) and anti-PD1-LTSL (Group 5) showed around a 2 – 3 fold increase in tumor-infiltrating CD8⁺ and CD4⁺ cells compared to the control group (Group 1) (**Figure 6C & 6D**). Interestingly, mice injected with mLTSL(DOX) (Group 4) also showed ~2 fold increase in the number of infiltrated CD8⁺ cells in the tumor compared to the control group (Group 1), where the latter is attributed to locally released DOX, inducing immunogenic cell death (ICD) and CD8⁺ T cell tumor infiltration [9-11].

Overall, our combined treatment showed a higher but not statistically significant difference compared to the mLTSL(DOX) (Group 4), which differs from our growth delay study, and the serum IFN- γ level. The discrepancy between our study and other reports [6, 32, 33] could be explained by a different route of administration (intravenous vs. intraperitoneal [34]) and the lower dose and frequency of administered anti-PD-1 mAb, which is 2-4 times lower than most studies, where a significant increase in tumor-infiltrating CD8⁺ T cells was reported [6, 16, 35]. Taking into account tumor temperature variations during irradiation, they could also cause fluctuations in the immune response among the treated mice. Furthermore, T cell isolation was carried out 3 and 6 days after the first and the second dosage, whilst the expansion and recruitment of memory CD8⁺ T cells require more than 7 days [36]. Finally, IFN- γ is a cytokine that is crucial for both innate and adaptive immunity and is secreted by a range of immune cells, such as activated CD8⁺ T cells [37], Th 1 CD4⁺ cells and natural killer cells [38], which have not been studied here, suggesting

that our treatment could activate a range of IFN- γ producing cells, leading to significant tumor inhibition.

Discussion

ThermoDox[®] is a low temperature-sensitive liposomal (LTSL) formulation encapsulating DOX. It has been clinically investigated to treat hepatic carcinoma in combination with radiofrequency ablation, and recently, in combination with high focused ultrasound (HIFU) [4]. Photothermal therapy is an alternative approach to treat cancer and trigger on-demand drug release [2, 39, 40]. Photothermal activation of LTSL(DOX) using near-infrared (NIR) fiber optics could offer an alternative and affordable approach to HIFU to treat accessible tumors. So far, LTSL have been loaded with photothermal agents, such as indocyanine green (ICG), where burst release of encapsulated DOX was achieved using mild, clinically attainable HT [41, 42]. In another study, Ou *et al.*, co-administered multi-branched gold nanoparticles with DOX-LTSL to trigger drug release *in vitro* [43]. Lately, IO NPs of different sizes have been seen as efficient heat mediators for photothermal therapy [44], using significantly lower IO NPs concentrations compared to magnetic hyperthermia [45] and with superior photothermal stability to liposomal ICG upon multiple irradiations [27, 46]. Furthermore, IO NPs have been used in combination with photothermal treatment and magnetic hyperthermia to potentiate cell killing [47, 48], highlighting new potentials of IO NPs in cancer therapy. Currently, neither magnetically- nor photothermally-activated LTSL have been reported, which could also enable MRI-image-guided drug delivery.

A few magnetoliposomes, incorporating hydrophobic IO NPs in the bilayer of conventional formulations, have been developed for MRI [49] or drug release [22, 50-52], where either slow or incomplete drug release was recorded in response to a magnetic field. However, there are no reports yet of mLTSL for MRI or burst drug release. Previously, we demonstrated the superiority of an 808 nm laser, compared to a magnetic field, to heat up minute concentrations of small IO NPs [45]. Herein, we demonstrated that the temperature rise of our mLTSL could be finely tuned by varying the iron concentration and the NIR laser power (**Figure 2A-D**). Furthermore, the work has been advanced to incorporate small hydrophobic IO NPs [19] into the LTSL lipid bilayer, where mild HT ($T_c \sim 42$ °C) was achieved using photothermal irradiation, resulting in efficient DOX release *in vitro* and *in vivo* (**Figure 2 & 4**). Taking into account the high photostability of

IO NPs [46] compared to LTSL-ICG [27], our mLTSL can also be utilized as a highly stable photothermal agent.

Besides their drug delivery and release capabilities, our mLTSL are seen as contrast agents with a higher relaxivity ($r_2 = 333 \text{ mM}^{-1} \text{ s}^{-1}$) than Resovist[®] ($r_2 = 189 \text{ mM}^{-1} \text{ s}^{-1}$) [53] (Table 2), which is currently available only in Japan. Embedding IO NPs from the same batch to the lipid bilayer (mLTSLs) significantly improved r_2 values compared to free, HCA-coated IO NPs ($r_2 = 3.2 \pm 0.8 \text{ mM}^{-1} \text{ s}^{-1}$). The reason lies in the differences in the fluidity and the diffusion dynamics of the water molecules into the secondary sphere of IO NPs. Recently, our group demonstrated the influence of the lipid bilayer fluidity on IO NPs relaxivity, where hydrophobic IO NPs embedded in fluid lipid bilayers served as better T_2 contrast agents compared to IO NPs incorporated in rigid lipid bilayers [19]. In agreement with this, the higher fluidity of LTSL exhibited higher relaxivity ($r_2 = 333 \text{ mM}^{-1} \text{ s}^{-1}$) than non-lysolipid containing DPPC:DSPE-PEG₂₀₀₀ liposomes ($r_2 = 283 \text{ mM}^{-1} \text{ s}^{-1}$) [19]. The superiority of mLTSL as a T_2 contrast agent has been demonstrated *in vivo* (Figure 5).

A massive effort has focused on understanding the role of tumor microenvironment in cancer progression, metastasis, and resistance to therapy [54, 55]. Immune checkpoint inhibitors, such as cytotoxic T lymphocyte-associated protein 4 (CTLA-4), PD1 and PD-L1 have been approved for the treatment of cancer by overcoming the immunosuppressive microenvironment [56]. Upregulated PD-L1 on cancer cells interacts with PD1 on the surface of infiltrated activated CD8⁺ cells and reduces the immune cell activity against cancer. Several anticancer approaches, such as photothermal therapy, and certain chemotherapeutics, such as DOX, trigger IFN- γ which induces PD-L1 overexpression on cancer cells and promote their survival [37, 57]. Therefore, combining a checkpoint blockade with some existing approaches has been seen as imperative in cancer therapy [5]. The bulk of existing research, in contrast to our study, has focused on enhancing the therapeutic efficacy of checkpoint inhibitors against non-immunogenic tumor and metastatic cancer by combining immunotherapy with photothermal therapy [6, 32, 33, 36, 56, 58-60]. In contrast, this present study aims to enhance the therapeutic efficacy of LTSL(DOX) via PD1 blockade.

DOX induces ICD (Figure S9) and recruits immune cells to the tumor sites [9-11]; however, upon the release of cytokines, PD-L1 is further overexpressed on the surface of cancer cells, leading to an immunosuppressive effect. In support of this, different studies have shown that

checkpoint inhibitors can potentiate the toxicity of DOX prodrug [14, 15] and Doxil® [16] but there are no reports yet of checkpoint inhibitors in combination with LTSL(DOX). Mild HT has also shown to trigger PD-L1 overexpression [6], which is an additional reason for combining immunotherapy with thermoresponsive liposomes. Thus, combining LTSL(DOX) with PD1/PD-L1 blockade, as our promising results in pre-clinical models showed, could enhance the therapeutic efficacy of LTSL(DOX) in patients by overcoming DOX and HT-induced PD-L1 expression. Furthermore, mLTSL(DOX) can be considered as a photothermal agent that could activate a systemic immune response against metastatic cancer [6]. The latter could be investigated in the future by comparing the therapeutic efficacy of PD1-LTSL combined with photothermally-activated mLTSL(DOX) to PD1-LTSL combined with conventional LTSL(DOX) and water bath hyperthermia against solid and metastatic tumor models.

PD-L1 overexpression is involved in a diverse array of tumor types because of its participation in signaling pathways regulating attenuated CD8⁺ T cell function and enhanced T_{reg} activity. Anti-PD1 mAb have shown evident anticancer activity by activating tumor-infiltrating cytotoxic T cells and depleting immunosuppressive tumor resident T_{reg} cells [61]. Anti-PD1 mAb have been used mainly in their soluble form, which could be associated with some systemic toxicity *in vivo*. To date, only one study has reported anti-PD1-functionalized liposomes, where anti-PD1 mAb was conjugated to conventional DOX-loaded liposomes to treat breast cancer [35]. Unfortunately, direct anti-PD1 mAb conjugation to our mLTSL was not technically possible in this study, as described previously; however, functionalizing mLTSL with anti-PD1 mAb using post-insertion methods, or incorporating anti-PD1-PEG₂₀₀₀-DSPE lipid to the initial formulation [35], could overcome this issue enabling engineering anti-PD1-mLTSL(DOX) theranostics. Nevertheless, our results showed that conjugating anti-PD1 mAb to LTSL maintained its binding to CD8⁺ T cells *in vitro* and its efficacy *in vivo*. Furthermore, the slowest tumor growth was observed in the mice treated with photothermally-activated mLTSL(DOX) and anti-PD1-LTSL (**Figure 6**), which was associated with a high level of systemic IFN- γ , and a slight increase in the total number of CD8⁺ and CD4⁺ T cells infiltrating the tumor. Previous studies showed that anti-PD1 mAb [61] and/or doxorubicin in its free or liposomal form [16] could deplete immunosuppressive T_{reg} cells from the tumor microenvironment, thus enhancing tumor immunogenicity. Furthermore, Rios-Doria *et al.*, showed that Doxil® had immunomodulatory effects on dendritic and immature myeloid cells in tumors [16]. Taking into account that we

analyzed the whole CD8⁺ and CD4⁺ T cells in the tumor, further studies are required to analyze the full immune cell profile (e.g. CD3⁺CD4⁺/ CD4⁺FOXP3⁺, macrophages, and MDSC) and ICD markers in tumors treated with photothermally-activated mLTSL(DOX) and anti-PD1 mAb.

Conclusions

Overall, we have engineered novel low temperature-sensitive magnetoliposomes (mLTSL) offering photothermally-induced burst DOX release and MR imaging. Furthermore anti-PD1 immunotherapy enhanced mLTSL(DOX) therapeutic efficacy *in vivo*.

ASSOCIATED CONTENT

Supporting Information. Characterization of IO NPs (TEM image with SAED and magnetic properties, Figure S1), superior MRI properties of our developed mLTSL temperature-sensitivity (Figure S2), T_2 -weighted MRI images were recorded for hydrophilic HCA-coated IO NPs and mLTSL containing different concentrations of Fe at 22 and 42 °C (Figure S3). Serum stability of DOX-loaded mLTSL (Figure S4), conjugation efficiency and physicochemical properties of anti-PD1-LTSL (Table S1), *in vitro* cytotoxicity of mLTSL (Figure S5), organs uptake of DOX-loaded mLTSL following intravenous administration and 808 nm laser irradiation (Figure S6), comparison of T_1 - and T_2 -weighted images for control groups and HCA-IO NPs and mLTSL treated mice 1h and 24h post-treatment (Figure S7), changes in body weight of CT26-tumor bearing mice (Figure S8), and DOX inducing ICD *in vitro* (Figure S9).

AUTHOR INFORMATION

Corresponding Author

*corresponding author: w.al-jamal@qub.ac.uk

Conflict of interest

The authors declare no conflict of interest

Funding Sources

Authors are grateful for financial support from Prostate Cancer UK (CDF-12-002 Fellowship), The Engineering and Physical Sciences Research Council (EPSRC) (EP/M008657/1), The Royal Society of London (RG2014 R1), and The Slovenian Research Agency ARRS (project numbers Z2-9218, P2-0084 and P3-0108). Ilaria Monaco spent six months (01-07-2015/ 31-12-2015) at the University of East Anglia, Norwich, UK, funded by “Marco Polo” fellowship (University of Bologna) during her PhD.

REFERENCES

- [1] K.M. Krishnan, Biomedical Nanomagnetism: A Spin Through Possibilities in Imaging, Diagnostics, and Therapy, *IEEE Trans. Magn.*, 46 (2010) 2523-2558, <https://doi.org/10.1109/tmag.2010.2046907>
- [2] G.A. Koning, A.M.M. Eggermont, L.H. Lindner, T.L.M. Ten Hagen, Hyperthermia and Thermosensitive Liposomes for Improved Delivery of Chemotherapeutic Drugs to Solid Tumors, *Pharm. Res.*, 27 (2010) 1750-1754, <https://doi.org/10.1007/s11095-010-0154-2>
- [3] M.-K. Yeh, I.C. Hsin, C. Ming-Yen, Clinical development of liposome based drugs: formulation, characterization, and therapeutic efficacy, *Int. J. Nanomed.*, (2011) 49, <https://doi.org/10.2147/ijn.s26766>
- [4] Y. Dou, K. Hynynen, C. Allen, To heat or not to heat: Challenges with clinical translation of thermosensitive liposomes, *J. Controlled Release*, 249 (2017) 63-73, <https://doi.org/10.1016/j.jconrel.2017.01.025>
- [5] H. Zhao, Y. Li, D. Wei, H. Luo, The Application of Nanoparticle-Based Drug Delivery Systems in Checkpoint Blockade Cancer Immunotherapy, *J. Immunol. Res.*, 2018 (2018) 3673295, <https://doi.org/10.1155/2018/3673295>
- [6] L. Huang, Y. Li, Y. Du, Y. Zhang, X. Wang, Y. Ding, X. Yang, F. Meng, J. Tu, L. Luo, C. Sun, Mild photothermal therapy potentiates anti-PD-L1 treatment for immunologically cold tumors via an all-in-one and all-in-control strategy, *Nat. Commun.*, 10 (2019) 4871, <https://doi.org/10.1038/s41467-019-12771-9>
- [7] G.K. Philips, M. Atkins, Therapeutic uses of anti-PD-1 and anti-PD-L1 antibodies, *Int. Immunol.*, 27 (2014) 39-46, <https://doi.org/10.1093/intimm/dxu095>
- [8] G. Kroemer, L. Galluzzi, O. Kepp, L. Zitvogel, Immunogenic cell death in cancer therapy, *Annu. Rev. Immunol.*, 31 (2013) 51-72, <https://doi.org/10.1146/annurev-immunol-032712-100008>
- [9] L. Apetoh, G. Mignot, T. Panaretakis, G. Kroemer, L. Zitvogel, Immunogenicity of anthracyclines: moving towards more personalized medicine, *Trends Mol. Med.*, 14 (2008) 141-151, <https://doi.org/10.1016/j.molmed.2008.02.002>
- [10] X. Li, The inducers of immunogenic cell death for tumor immunotherapy, *Tumori J.*, 104 (2018) 1-8, <https://doi.org/10.5301/tj.5000675>
- [11] J. Pol, E. Vacchelli, F. Aranda, F. Castoldi, A. Eggermont, I. Cremer, C. Sautes-Fridman, J. Fucikova, J. Galon, R. Spisek, E. Tartour, L. Zitvogel, G. Kroemer, L. Galluzzi, Trial Watch: Immunogenic cell death inducers for anticancer chemotherapy, *Oncoimmunology*, 4 (2015) e1008866, <https://doi.org/10.1080/2162402X.2015.1008866>
- [12] K.-C. Mei, Y.-P. Liao, J. Jiang, M. Chiang, M. Khazaieli, X. Liu, X. Wang, Q. Liu, C.H. Chang, X. Zhang, J. Li, Y. Ji, B. Melano, D. Telesca, T. Xia, H. Meng, A.E. Nel, Liposomal Delivery of Mitoxantrone and a Cholesteryl Indoximod Prodrug Provides Effective Chemo-immunotherapy in Multiple Solid Tumors, *ACS Nano*, 14 (2020) 13343-13366, <https://doi.org/10.1021/acsnano.0c05194>
- [13] Y. Gilad, Y. Eliaz, Y. Yu, S.J. Han, B.W. O'Malley, D.M. Lonard, Drug-induced PD-L1 expression and cell stress response in breast cancer cells can be balanced by drug combination, *Sci. Rep.*, 9 (2019), <https://doi.org/10.1038/s41598-019-51537-7>
- [14] J. Wei, Y. Long, R. Guo, X. Liu, X. Tang, J. Rao, S. Yin, Z. Zhang, M. Li, Q. He, Multifunctional polymeric micelle-based chemo-immunotherapy with immune checkpoint blockade for efficient treatment of orthotopic and metastatic breast cancer, *Acta Pharm. Sin. B*, 9 (2019) 819-831, <https://doi.org/10.1016/j.apsb.2019.01.018>

- [15] L. Hu, Z. Cao, L. Ma, Z. Liu, G. Liao, J. Wang, S. Shen, D. Li, X. Yang, The potentiated checkpoint blockade immunotherapy by ROS-responsive nanocarrier-mediated cascade chemophotodynamic therapy, *Biomaterials*, 223 (2019) 119469, <https://doi.org/10.1016/j.biomaterials.2019.119469>
- [16] J. Rios-Doria, N. Durham, L. Wetzel, R. Rothstein, J. Chesebrough, N. Holoweckyj, W. Zhao, C.C. Leow, R. Hollingsworth, Doxil synergizes with cancer immunotherapies to enhance antitumor responses in syngeneic mouse models, *Neoplasia*, 17 (2015) 661-670, <https://doi.org/10.1016/j.neo.2015.08.004>
- [17] W.T. Al-Jamal, Z.S. Al-Ahmady, K. Kostarelos, Pharmacokinetics & tissue distribution of temperature-sensitive liposomal doxorubicin in tumor-bearing mice triggered with mild hyperthermia, *Biomaterials*, 33 (2012) 4608-4617, <https://doi.org/https://doi.org/10.1016/j.biomaterials.2012.03.018>
- [18] M.A. Santos, D.E. Goertz, K. Hynynen, Focused Ultrasound Hyperthermia Mediated Drug Delivery Using Thermosensitive Liposomes and Visualized With in vivo Two-Photon Microscopy, *Theranostics*, 7 (2017) 2718-2731, <https://doi.org/10.7150/thno.19662>
- [19] N. Kostevsek, C.C.L. Cheung, I. Sersa, M.E. Kreft, I. Monaco, M. Comes Franchini, J. Vidmar, W.T. Al-Jamal, Magneto-Liposomes as MRI Contrast Agents: A Systematic Study of Different Liposomal Formulations, *Nanomaterials (Basel)*, 10 (2020), <https://doi.org/10.3390/nano10050889>
- [20] A. Fritze, F. Hens, A. Kimpfler, R. Schubert, R. Peschka-Süss, Remote loading of doxorubicin into liposomes driven by a transmembrane phosphate gradient, *Biochimica et Biophysica Acta (BBA) - Biomembranes*, 1758 (2006) 1633-1640, <https://doi.org/10.1016/j.bbamem.2006.05.028>
- [21] M.P. Morales, S. Veintemillas-Verdaguer, C.J. Serna, Magnetic properties of uniform γ -Fe₂O₃ nanoparticles smaller than 5 nm prepared by laser pyrolysis, *J. Mater. Res.*, 14 (1999) 3066-3072, <https://doi.org/10.1557/JMR.1999.0411>
- [22] E. Amstad, J. Kohlbrecher, E. Müller, T. Schweizer, M. Textor, E. Reimhult, Triggered Release from Liposomes through Magnetic Actuation of Iron Oxide Nanoparticle Containing Membranes, *Nano Lett.*, 11 (2011) 1664-1670, <https://doi.org/10.1021/nl2001499>
- [23] P. Caravan, J.J. Ellison, T.J. McMurphy, R.B. Lauffer, Gadolinium(III) Chelates as MRI Contrast Agents: Structure, Dynamics, and Applications, *Chem. Rev.*, 99 (1999) 2293-2352, <https://doi.org/10.1021/cr980440x>
- [24] N. Kostevšek, S. Hudoklin, M.E. Kreft, I. Serša, A. Sepe, Z. Jagličić, J. Vidmar, J. Ščančar, S. Šturm, S. Kobe, K. Žužek Rožman, Magnetic interactions and in vitro study of biocompatible hydrocaffeic acid-stabilized Fe-Pt clusters as MRI contrast agents, *RSC Advances*, 8 (2018) 14694-14704, <https://doi.org/10.1039/C8RA00047F>
- [25] Y.-X.J. Wang, Superparamagnetic iron oxide based MRI contrast agents: Current status of clinical application, *Quantitative Imaging in Medicine and Surgery*, 1 (2011) 35-40,
- [26] A. Jain, S.K. Jain, Chapter 9 - Application Potential of Engineered Liposomes in Tumor Targeting, in: A.M. Grumezescu (Ed.) *Multifunctional Systems for Combined Delivery, Biosensing and Diagnostics*, Elsevier, 2017, pp. 171-191.
- [27] C.C.L. Cheung, G. Ma, K. Karatasos, J. Seitsonen, J. Ruokolainen, C.R. Koffi, H. Hassan, W.T. Al-Jamal, Liposome-Templated Indocyanine Green J- Aggregates for In Vivo Near-Infrared Imaging and Stable Photothermal Heating, *Nanotheranostics*, 4 (2020) 91-106, <https://doi.org/10.7150/ntno.41737>
- [28] N. Beziere, N. Lozano, A. Nunes, J. Salichs, D. Queiros, K. Kostarelos, V. Ntziachristos, Dynamic imaging of PEGylated indocyanine green (ICG) liposomes within the tumor

microenvironment using multi-spectral optoacoustic tomography (MSOT), *Biomaterials*, 37 (2015) 415-424, <https://doi.org/10.1016/j.biomaterials.2014.10.014>

[29] C.W. Song, Effect of Local Hyperthermia on Blood Flow and Microenvironment: A Review, *Cancer Res.*, 44 (1984) 4721s,

[30] R.M. Lowenthal, K. Eaton, TOXICITY OF CHEMOTHERAPY, *Hematology/Oncology Clinics of North America*, 10 (1996) 967-990, [https://doi.org/10.1016/s0889-8588\(05\)70378-6](https://doi.org/10.1016/s0889-8588(05)70378-6)

[31] Q. Chen, A. Krol, A. Wright, D. Needham, M.W. Dewhirst, F. Yuan, Tumor microvascular permeability is a key determinant for antivascular effects of doxorubicin encapsulated in a temperature sensitive liposome, *Int. J. Hyperthermia*, 24 (2008) 475-482, <https://doi.org/10.1080/02656730701854767>

[32] Q. Chen, L. Xu, C. Liang, C. Wang, R. Peng, Z. Liu, Photothermal therapy with immune-adjuvant nanoparticles together with checkpoint blockade for effective cancer immunotherapy, *Nat. Commun.*, 7 (2016) 13193, <https://doi.org/10.1038/ncomms13193>

[33] J. Nam, S. Son, L.J. Ochyl, R. Kuai, A. Schwendeman, J.J. Moon, Chemo-photothermal therapy combination elicits anti-tumor immunity against advanced metastatic cancer, *Nat. Commun.*, 9 (2018) 1074, <https://doi.org/10.1038/s41467-018-03473-9>

[34] T.Y. Huang, G.L. Huang, C.Y. Zhang, B.W. Zhuang, B.X. Liu, L.Y. Su, J.Y. Ye, M. Xu, M. Kuang, X.Y. Xie, Supramolecular Photothermal Nanomedicine Mediated Distant Tumor Inhibition via PD-1 and TIM-3 Blockage, *Front. Chem.*, 8 (2020) 1, <https://doi.org/10.3389/fchem.2020.00001>

[35] Y. Du, X. Liang, Y. Li, T. Sun, Z. Jin, H. Xue, J. Tian, Nuclear and Fluorescent Labeled PD-1-Liposome-DOX-64Cu/IRDye800CW Allows Improved Breast Tumor Targeted Imaging and Therapy, *Mol. Pharmaceutics*, 14 (2017) 3978-3986, <https://doi.org/10.1021/acs.molpharmaceut.7b00649>

[36] K. Ektate, M.C. Munteanu, H. Ashar, J. Malayer, A. Ranjan, Chemo-immunotherapy of colon cancer with focused ultrasound and Salmonella-laden temperature sensitive liposomes (thermobots), *Sci. Rep.*, 8 (2018) 13062, <https://doi.org/10.1038/s41598-018-30106-4>

[37] K. Abiko, N. Matsumura, J. Hamanishi, N. Horikawa, R. Murakami, K. Yamaguchi, Y. Yoshioka, T. Baba, I. Konishi, M. Mandai, IFN-gamma from lymphocytes induces PD-L1 expression and promotes progression of ovarian cancer, *Br. J. Cancer*, 112 (2015) 1501-1509, <https://doi.org/10.1038/bjc.2015.101>

[38] P. Bhat, G. Leggatt, N. Waterhouse, I.H. Frazer, Interferon- γ derived from cytotoxic lymphocytes directly enhances their motility and cytotoxicity, *Cell Death Dis.*, 8 (2017) e2836-e2836, <https://doi.org/10.1038/cddis.2017.67>

[39] M.B.C. De Matos, N. Beztsinna, C. Heyder, M.H.A.M. Fens, E. Mastrobattista, R.M. Schiffelers, G. Lenewit, R.J. Kok, Thermosensitive liposomes for triggered release of cytotoxic proteins, *European Journal of Pharmaceutics and Biopharmaceutics*, 132 (2018) 211-221, <https://doi.org/10.1016/j.ejpb.2018.09.010>

[40] S.M. Park, M.S. Kim, S.J. Park, E.S. Park, K.S. Choi, Y.S. Kim, H.R. Kim, Novel temperature-triggered liposome with high stability: formulation, in vitro evaluation, and in vivo study combined with high-intensity focused ultrasound (HIFU), *J Control Release*, 170 (2013) 373-379, <https://doi.org/10.1016/j.jconrel.2013.06.003>

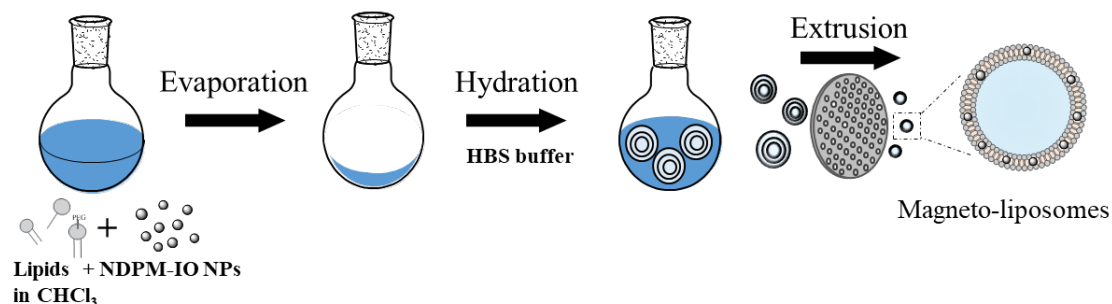
[41] T. Lajunen, L.-S. Kontturi, L. Viitala, M. Manna, O. Cramariuc, T. Róg, A. Bunker, T. Laaksonen, T. Viitala, L. Murtomäki, A. Urtti, Indocyanine Green-Loaded Liposomes for Light-Triggered Drug Release, *Mol. Pharmaceutics*, 13 (2016) 2095-2107, <https://doi.org/10.1021/acs.molpharmaceut.6b00207>

- [42] C.C.L. Au - Cheung, G. Au - Ma, A. Au - Ruiz, W.T. Au - Al-Jamal, Microfluidic Production of Lysolipid-Containing Temperature-Sensitive Liposomes, *JoVE*, (2020) e60907, <https://doi.org/doi:10.3791/60907>
- [43] Y.-C. Ou, J.A. Webb, S. Faley, D. Shae, E.M. Talbert, S. Lin, C.C. Cutright, J.T. Wilson, L.M. Bellan, R. Bardhan, Gold Nanoantenna-Mediated Photothermal Drug Delivery from Thermosensitive Liposomes in Breast Cancer, *1* (2016) 234-243, <https://doi.org/10.1021/acsomega.6b00079>
- [44] S. Shen, S. Wang, R. Zheng, X. Zhu, X. Jiang, D. Fu, W. Yang, Magnetic nanoparticle clusters for photothermal therapy with near-infrared irradiation, *Biomaterials*, *39* (2015) 67-74, <https://doi.org/10.1016/j.biomaterials.2014.10.064>
- [45] J. Hu, A. Dehsorkhi, W. Al-Jamal, Y. Zhang, S. Chen, C. Yang, D. Tan, Q. Zhao, C. Yang, Y. Wang, Studies on the Photothermal Effect of PEGylated Fe₃O₄ Nanoparticles, *Nanoscience and Nanotechnology Letters*, *9* (2017) 556-561, <https://doi.org/10.1166/nnl.2017.2355>
- [46] N. Zhang, J. Song, Y. Liu, M. Liu, L. Zhang, D. Sheng, L. Deng, H. Yi, M. Wu, Y. Zheng, Z. Wang, Z. Yang, Photothermal therapy mediated by phase-transformation nanoparticles facilitates delivery of anti-PD1 antibody and synergizes with antitumor immunotherapy for melanoma, *J. Controlled Release*, *306* (2019) 15-28, <https://doi.org/10.1016/j.jconrel.2019.05.036>
- [47] A. Espinosa, R. Di Corato, J. Kolosnjaj-Tabi, P. Flaud, T. Pellegrino, C. Wilhelm, Duality of Iron Oxide Nanoparticles in Cancer Therapy: Amplification of Heating Efficiency by Magnetic Hyperthermia and Photothermal Bimodal Treatment, *ACS Nano*, *10* (2016) 2436-2446, <https://doi.org/10.1021/acsnano.5b07249>
- [48] A. Espinosa, M. Bugnet, G. Radtke, S. Neveu, G.A. Botton, C. Wilhelm, A. Abou-Hassan, Can magneto-plasmonic nanohybrids efficiently combine photothermia with magnetic hyperthermia?, *7* (2015) 18872-18877, <https://doi.org/10.1039/c5nr06168g>
- [49] R. Martínez-González, J. Estelrich, M. Busquets, Liposomes Loaded with Hydrophobic Iron Oxide Nanoparticles: Suitable T2 Contrast Agents for MRI, *Int. J. Mol. Sci.*, *17* (2016) 1209, <https://doi.org/10.3390/ijms17081209>
- [50] M. Bañobre-López, A. Teijeiro, J. Rivas, Magnetic nanoparticle-based hyperthermia for cancer treatment, *Reports of Practical Oncology & Radiotherapy*, *18* (2013) 397-400, <https://doi.org/10.1016/j.rpor.2013.09.011>
- [51] Y. Chen, A. Bose, G.D. Bothun, Controlled Release from Bilayer-Decorated Magnetoliposomes via Electromagnetic Heating, *ACS Nano*, *4* (2010) 3215-3221, <https://doi.org/10.1021/nn100274v>
- [52] A. Salvatore, C. Montis, D. Berti, P. Baglioni, Multifunctional Magnetoliposomes for Sequential Controlled Release, *10* (2016) 7749-7760, <https://doi.org/10.1021/acsnano.6b03194>
- [53] S.M. Dadfar, K. Roemhild, N.I. Drude, S. Von Stillfried, R. Knüchel, F. Kiessling, T. Lammers, Iron oxide nanoparticles: Diagnostic, therapeutic and theranostic applications, *Adv. Drug Delivery Rev.*, *138* (2019) 302-325, <https://doi.org/10.1016/j.addr.2019.01.005>
- [54] P. Allavena, A. Mantovani, Immunology in the clinic review series; focus on cancer: tumour-associated macrophages: undisputed stars of the inflammatory tumour microenvironment, *Clinical & Experimental Immunology*, *167* (2012) 195-205, <https://doi.org/10.1111/j.1365-2249.2011.04515.x>
- [55] W. Zou, L. Chen, Inhibitory B7-family molecules in the tumour microenvironment, *Nature Reviews Immunology*, *8* (2008) 467-477, <https://doi.org/10.1038/nri2326>
- [56] X. Liu, J. Zheng, W. Sun, X. Zhao, Y. Li, N. Gong, Y. Wang, X. Ma, T. Zhang, L.Y. Zhao, Y. Hou, Z. Wu, Y. Du, H. Fan, J. Tian, X.J. Liang, Ferrimagnetic Vortex Nanoring-Mediated Mild

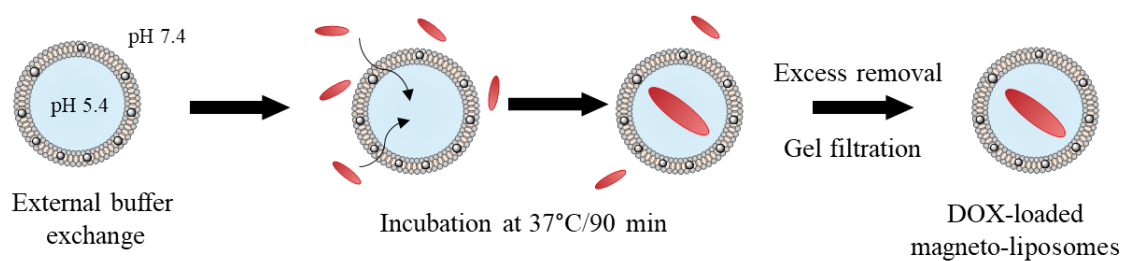
- Magnetic Hyperthermia Imparts Potent Immunological Effect for Treating Cancer Metastasis, *ACS Nano*, 13 (2019) 8811-8825, <https://doi.org/10.1021/acsnano.9b01979>
- [57] C. Blank, I. Brown, A.C. Peterson, M. Spiotto, Y. Iwai, T. Honjo, T.F. Gajewski, PD-L1/B7H-1 Inhibits the Effector Phase of Tumor Rejection by T Cell Receptor (TCR) Transgenic CD8+T Cells, *Cancer Res.*, 64 (2004) 1140-1145, <https://doi.org/10.1158/0008-5472.can-03-3259>
- [58] C. Wang, L. Xu, C. Liang, J. Xiang, R. Peng, Z. Liu, Immunological responses triggered by photothermal therapy with carbon nanotubes in combination with anti-CTLA-4 therapy to inhibit cancer metastasis, *Adv. Mater.*, 26 (2014) 8154-8162, <https://doi.org/10.1002/adma.201402996>
- [59] Y. Liu, P. Maccarini, G.M. Palmer, W. Etienne, Y. Zhao, C.T. Lee, X. Ma, B.A. Inman, T. Vo-Dinh, Synergistic Immuno Photothermal Nanotherapy (SYMPHONY) for the Treatment of Unresectable and Metastatic Cancers, *Sci Rep*, 7 (2017) 8606, <https://doi.org/10.1038/s41598-017-09116-1>
- [60] W. Chen, Z. Guo, Y. Zhu, N. Qiao, Z. Zhang, X. Sun, Combination of Bacterial - Photothermal Therapy with an Anti - PD - 1 Peptide Depot for Enhanced Immunity against Advanced Cancer, *Adv. Funct. Mater.*, (2019), <https://doi.org/10.1002/adfm.201906623>
- [61] K. Yoshida, M. Okamoto, J. Sasaki, C. Kuroda, H. Ishida, K. Ueda, H. Ideta, T. Kamanaka, A. Sobajima, T. Takizawa, M. Tanaka, K. Aoki, T. Uemura, H. Kato, H. Haniu, N. Saito, Anti-PD-1 antibody decreases tumour-infiltrating regulatory T cells, *BMC Cancer*, 20 (2020), <https://doi.org/10.1186/s12885-019-6499-y>

Figures and captions

(A) Formulation of magneto-liposomes



(B) pH-gradient DOX loading



Scheme 1. Schematic representation of mLTSL(DOX) preparation. (A) Preparation of the formulation of mLTSL using a thin-film hydration and extrusion method and (B) Doxorubicin (DOX) loading into the mLTSL aqueous core using the pH-gradient method.

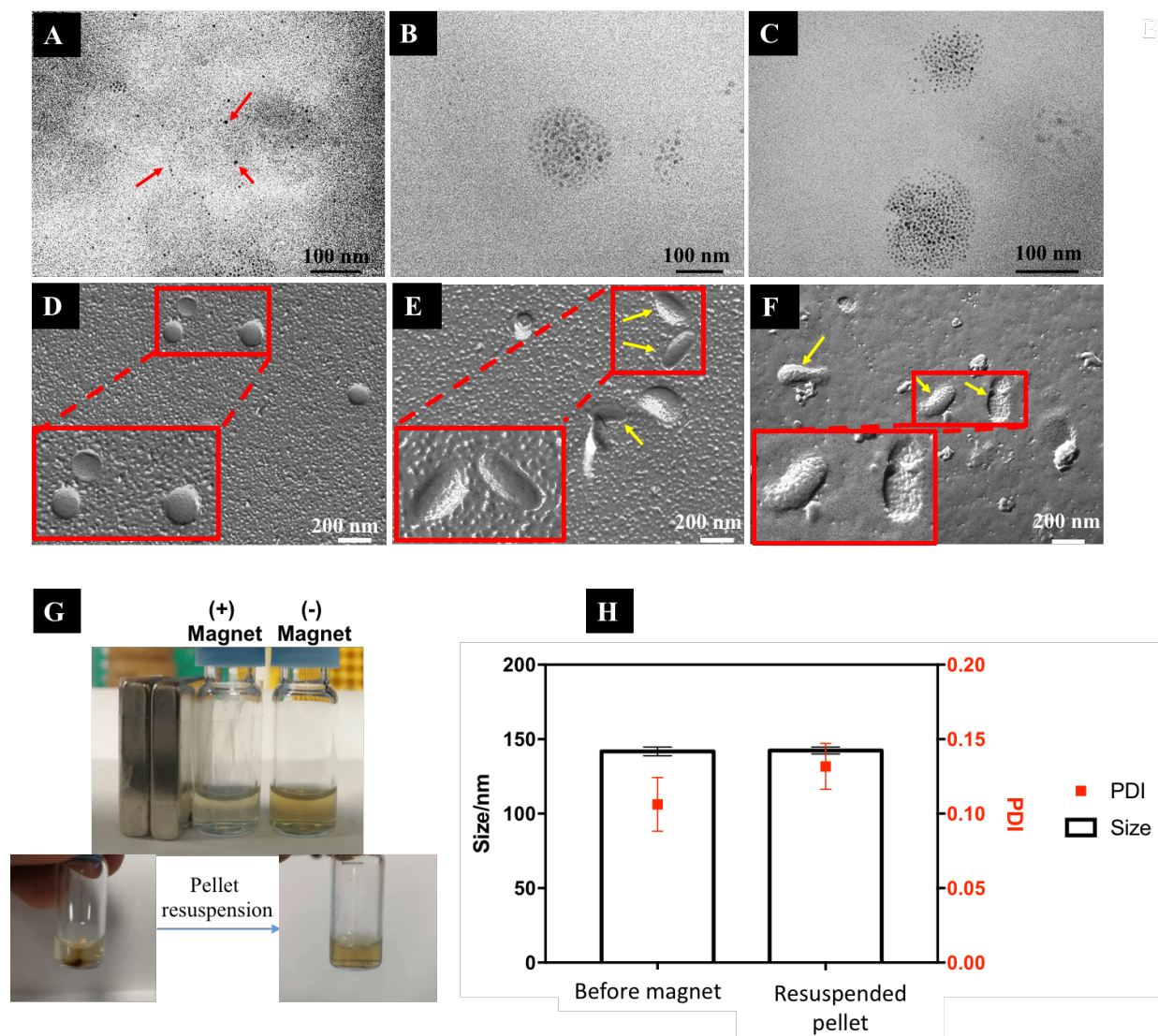


Figure 1. Structural characterization and colloidal stability of mLTSL. TEM images of mLTSL prepared with NDPM-coated IO NPs: lipid ratio of (A) 10, (B) 20, (C) 30 g/mol. FF-EM images of (D) empty LTSL, (E) LTSL(DOX), and (F) mLTSL(DOX) (NDPM IO NPs: lipid ratio of 30 g/mol). Elongated vesicles were observed in (E & F) following DOX loading, indicating the formation of DOX crystals. Rough vesicles observed in (F) represent hydrophobic IO NPs embedded in LTSL. The red boxes insets magnify selected particles. All TEM images were captured without negative staining. (G) Images of mLTSL dispersions exposed to a magnetic field (top, left), where a magnetically attracted pellet was re-dispersed, showing good colloidal stability (bottom). (H) The hydrodynamic diameter and PDI of mLTSL before and after magnetic exposure.

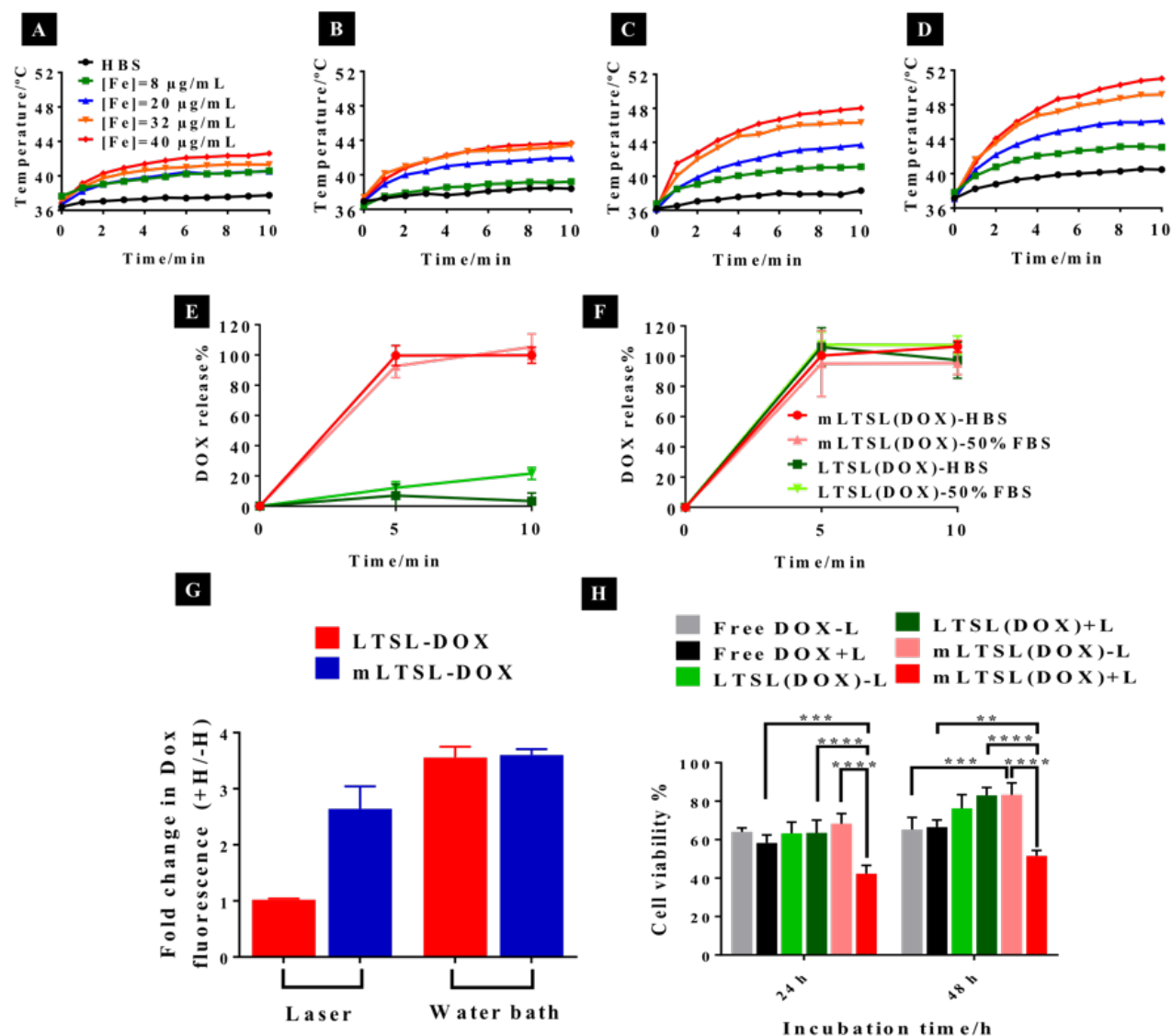


Figure 2. Photothermal heating capacity of mLTSL and *in vitro* DOX release and toxicity using an 808 nm laser. Temperature increase of mLTSL dispersions containing different concentrations of Fe (HBS: black dots, 8 µg/mL: green squares, 20 µg/mL: blue triangles, 32 µg/mL: orange down triangles, 40 µg/mL: red diamonds) following the exposure to an 808 nm laser of (A) 0.55, (B) 0.77, (C) 1.31, (D) 1.7 W/cm². HBS was used as a control. DOX release profile of LTSL and mLTSL ([Fe]=20 µg/mL) in HBS and 50% FBS, using (E) 808 nm laser (1.31 W/cm²) and (F) 42°C water bath. Data is shown as mean ± SD (n = 3). (G) *In vitro* DOX release in CT26 cells. A fold change of DOX fluorescence was determined by measuring the fold increase in DOX fluorescence following HT treatment using 808 nm laser (1.7 W/cm²; 5 min) or water bath (42°C, 1 hour) to 37 °C. Cells were treated with 2 µM

of LTSL(DOX), and mL TSL(DOX) ([Fe]=40 µg/mL) followed by HT conditions described above, were incubated at 37 °C/5 % CO₂. Flow cytometry analysis of all samples were carried out 2 hours later. Data is shown as mean ± SD (n = 3). **(H)** To determine the *in vitro* cytotoxicity of mL TSL(DOX), CT26 cells (1 x 10⁴ /well) were seeded overnight in a 96 well-plate. Cells were incubated with mL TSL(DOX) ([Fe] = 20 µg/mL), LTSL(DOX), and free DOX at an equivalent dose of 1 µM DOX with/without laser (808 nm, 1.7 W/cm², 5 min) treatment, and 4 hours later, cells were washed and replenished with fresh complete media, then returned to 37 °C/5 % CO₂ for another 20 or 44 hours. Cell viability was assessed using resazurin assay. Results are expressed as a percentage of non-treated cells. Data is shown as mean ± SD (n = 6). One-way ANOVA was performed for statistical analysis, differences were considered significant at p < 0.05 (*p < 0.05, **p < 0.01, ***p < 0.001, ****p < 0.0001).

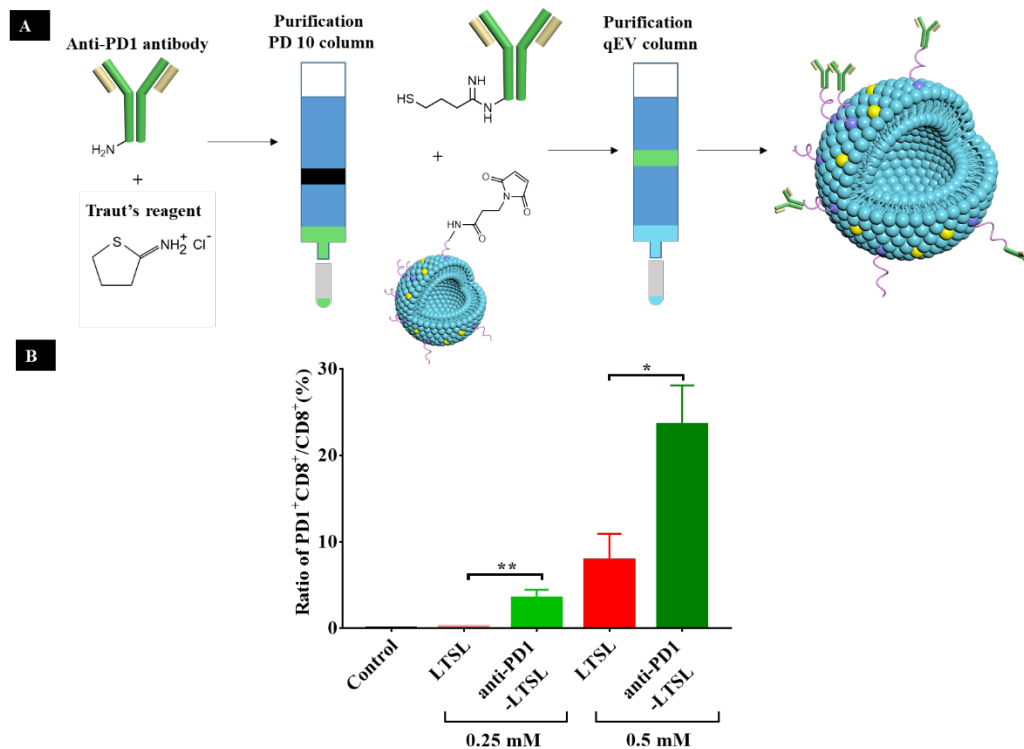


Figure 3. The binding capacity of anti-PD1-LTSL to CD8⁺ cells. (A) Schematic presentation of anti-PD1-LTSL preparation. **(B)** Splenocytes were collected from C57BL/6 mice and seeded in a 12-well plate (0.5 million/well). Then 1 mL of fluorescently-DiI-labeled, PD1-LTSL (3 μ g PD1 mAb/0.25 μ mol lipid or 6 μ g PD1 mAb/0.5 μ mol lipid) or equivalent non-targeted LTSL were added to the wells. 3 hours post-incubation, the binding capacity of anti-PD1 antibody conjugated LTSL to CD8⁺ cells population was studied using flow cytometry, by calculating the percentage ratio of PD1⁺CD8⁺ to CD8⁺ cells. Data is shown as mean \pm SD (n = 3). **Statistical analysis was performed by unpaired two-tail Student's t-test, differences were considered significant at $p < 0.05$, * $p < 0.05$, ** $p < 0.01$.**

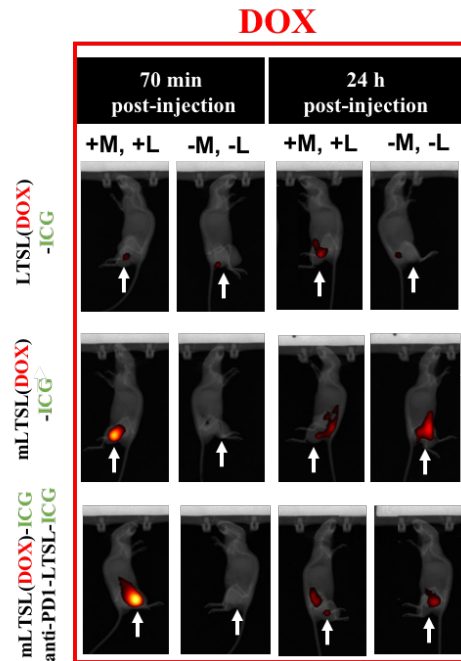
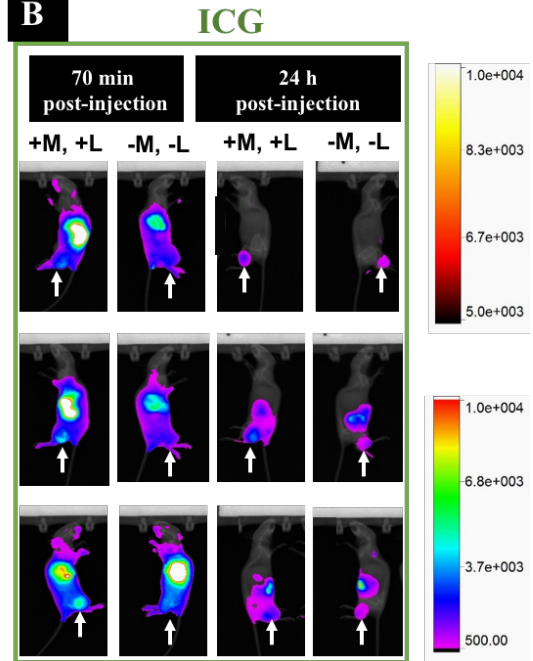
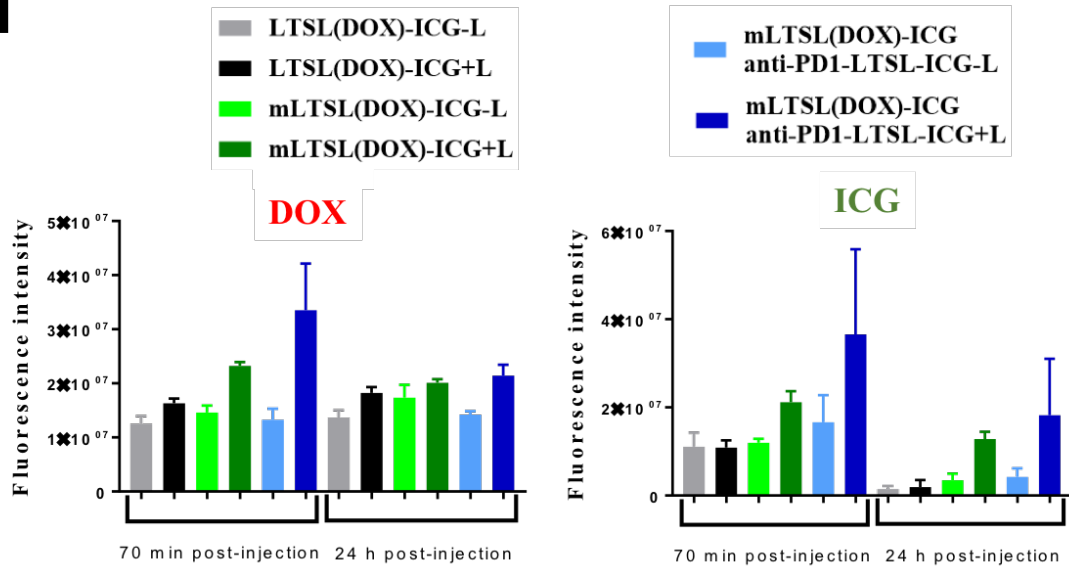
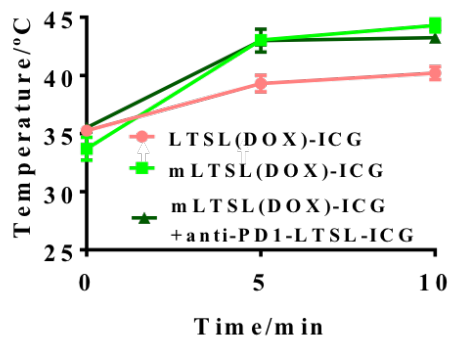
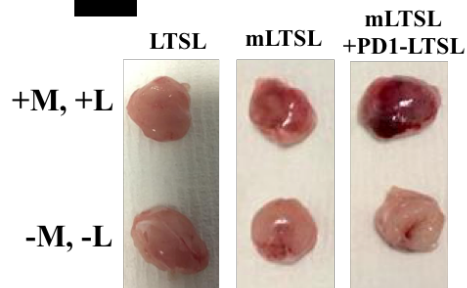
A**B****C****D****E**

Figure 4. Photothermal-induced mLTSL(DOX) release *in vivo*. CT26 tumor-bearing mice (bifocal tumors were implanted on the legs) were i.v. injected with LTSL(DOX)-ICG, mLTSL(DOX)-ICG, and mLTSL(DOX)-ICG+anti-PD1-LTSL-ICG (two formulations were mixed and injected together) at a dose of DOX:160 µg, ICG: 10 µg, Fe: 60 µg, anti-PD1 mAb: 50 µg per mouse. After injection, one tumor was immediately taped with a magnet for 50 minutes and irradiated with the laser (808 nm, 0.3 W/cm²) for 10 minutes (+M, +L). Non-irradiated tumors were labeled as (-M, -L). Live fluorescence imaging was carried out immediately and 24 hours post-laser treatment. Whole body fluorescence of (A) DOX and (B) ICG following tumor irradiation (white arrows indicate the tumor positions on the leg). (C) DOX (top) and ICG (bottom) tumor quantification in living mice (n=3). (D) Tumors' temperatures during laser irradiation were recorded by a thermal camera. (E) Images of isolated tumors from mice injected with the formulations described above in the presence (+M, +L) and absence of (-M, -L) of laser treatment.

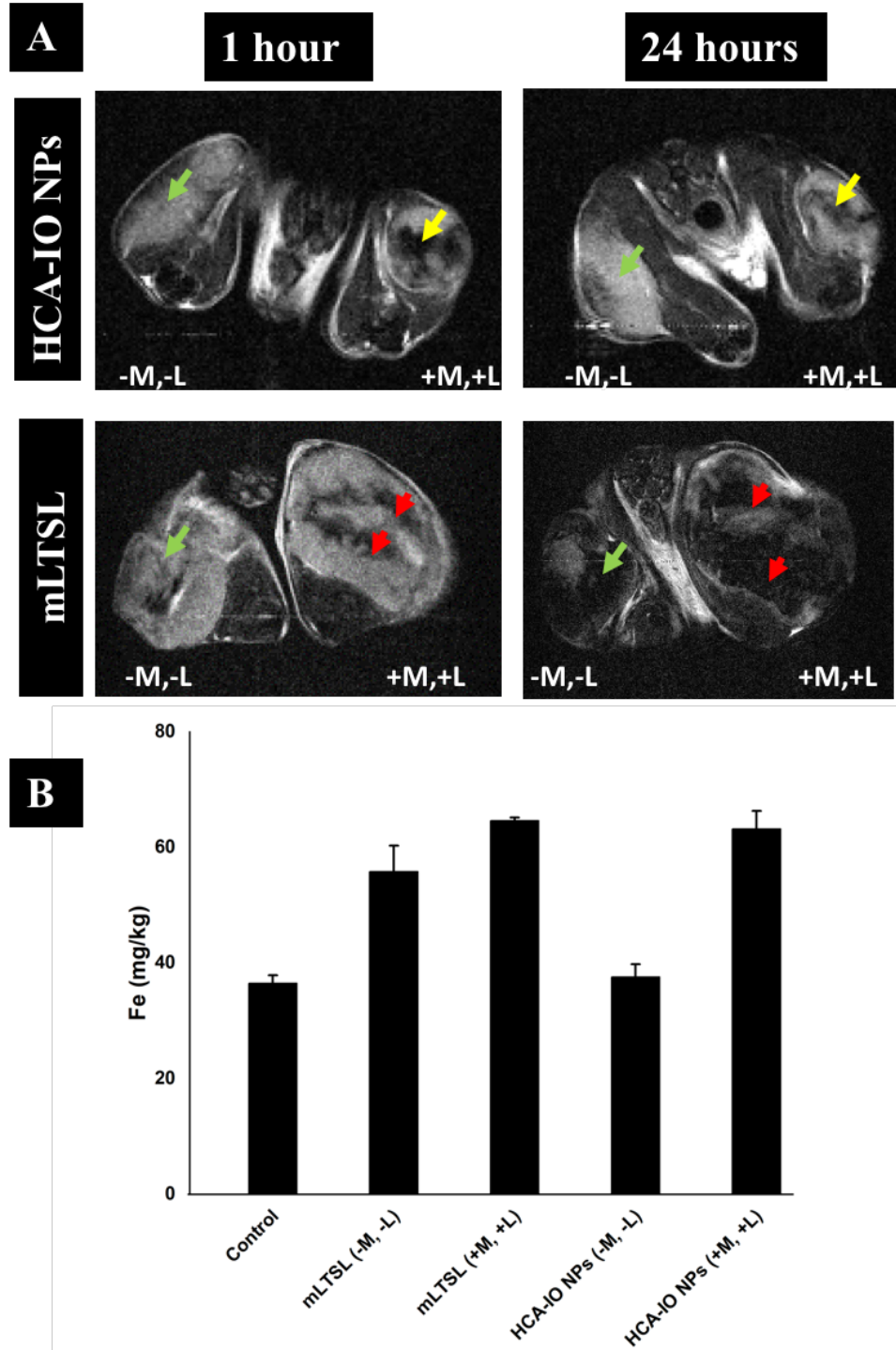


Figure 5. mLTSL as efficient *T*₂ contrast agents *in vivo*. CT26 tumor-bearing mice were intravenously injected with HCA-IO NPs or mLTSL at a Fe dose of 50 μ g per mouse. After injection, one tumor was immediately taped with a magnet for 50 minutes and irradiated with the laser (808 nm, 0.3 W/cm²) for 10 minutes (+M,+L). The second tumor was not exposed to a magnet and was not irradiated (-M, -L). (A) *T*₂-weighted images were taken 1 hour and 24 hours post-injection. Red and yellow arrows indicate darker contrast in treated tumors (+M, +L) injected with mLTSL and

HCA-IO NPs, respectively. Green arrows indicate non-treated tumors (-M, -L). T_2 -weighted MR images were recorded using the following sequences TE/TR = 40/3000 ms. (B) Fe concentration in CT26 tumors 24 hours post-treatment. The tumors were analyzed using ICP-MS, and the values are expressed as Fe mg per tumor mass (kg).

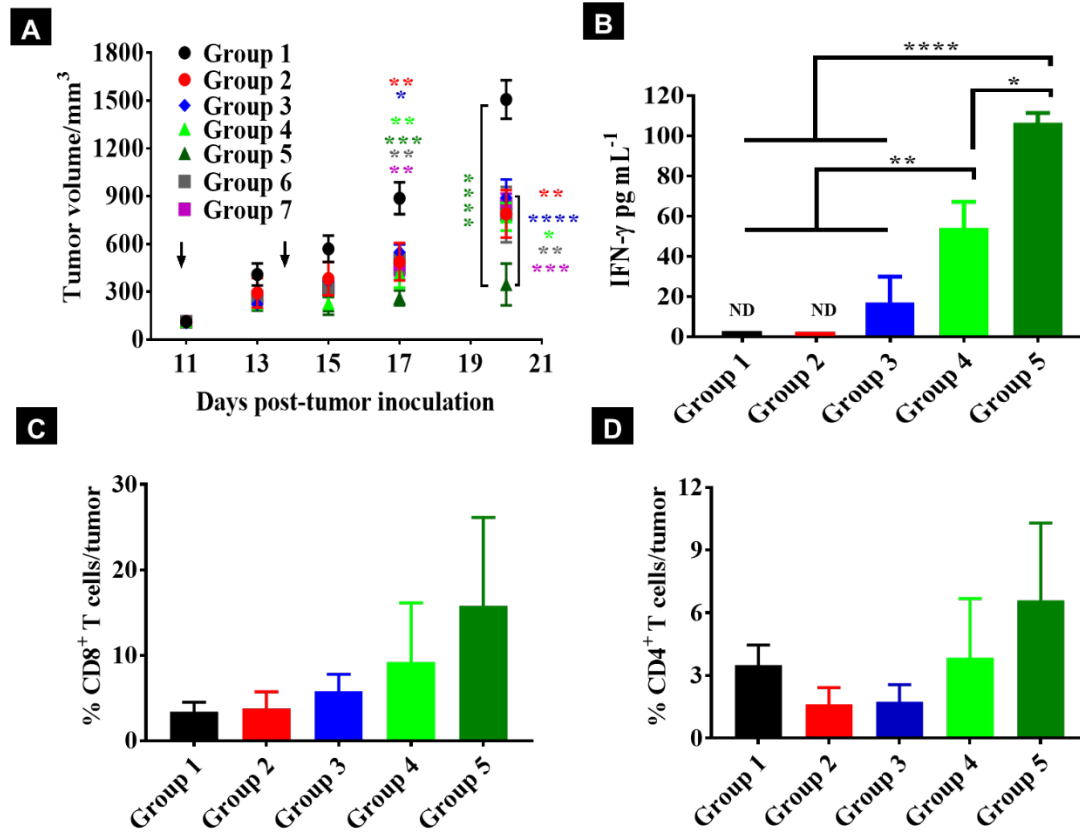


Figure 6. Tumor growth delay and immune response in mice treated with DOX-loaded mLTSL/anti-PD1-LTSL in combination with an 808 nm laser. (A) Growth curves of CT26 tumor inoculated subcutaneously in BALB/c mice, and intravenously injected with PBS (Group 1, control, black dots), free DOX (Group 2, 2 mg/kg, red dots), anti-PD1 mAb (Group 3, 2.5 mg/kg, blue diamonds), mLTSL(DOX) (Group 4, DOX: 2 mg/kg, Fe: 3 mg/kg, light green triangles), mLTSL (DOX)+anti-PD1-LTSL (Group 5, DOX: 2 mg/kg, Fe: 3 mg/kg, anti-PD1 mAb: 2.5 mg/kg, dark green triangles), LTSL (DOX) (Group 6, DOX: 2 mg/kg, grey squares), and LTSL (DOX)+anti-PD1-LTSL (Group 7, DOX: 2 mg/kg, anti-PD1 mAb: 2.5 mg/kg, purple squares). After injection, a magnet disc was taped to the tumor for 50 minutes followed by 808 nm laser irradiation (0.3 W/cm² for 10 minutes) in all the groups. Black arrows indicate the days of treatment (day 11 & 14). Data are expressed as the mean \pm SEM (n=5). (B) Serum IFN- γ , (C) percentage of CD8⁺ T cells, and (D) percentage of CD4⁺ T cells infiltrated into the tumor of mice treated with PBS (Group 1, control), free DOX (Group 2, 2 mg/kg), anti-PD1 mAb (Group 3, 2.5 mg/kg), mLTSL(DOX) (Group 4, DOX: 2 mg/kg, Fe: 3 mg/kg), mLTSL (DOX)+anti-PD1-LTSL (Group 5, DOX: 2 mg/kg, Fe: 3 mg/kg, anti-PD1 mAb: 2.5 mg/kg). For the immune response study, mice were injected twice (day 11 & 14), and the serum and tumor CD8⁺ T and CD4⁺ T cells were collected 72 hours after the second injection. Data are expressed as the mean \pm SEM (n = 3). Statistical analysis was performed by one-way ANOVA, *p<0.05, **p<0.01, ***p<0.001, ****p<0.0001. ND: none detectable.

Table 1. Physicochemical properties of mLTSL(DOX) and anti-PD-LTSL. Hydrodynamic size, polydispersity index (PDI), zeta potential of mLTSL(DOX) prepared with different lipid-to-NPs ratios were determined using DLS. NPs encapsulation efficiency (%EE) and Fe content measured using AAS. Lipid phase transition temperature and doxorubicin encapsulation efficiency (DOX %EE) were determined using DSC and a fluorescence plate reader, respectively.

NPs-to-Lipid [g/mol]	NP %EE± SD	Fe-to-Lipid ± SD [g/mol]	Size ± SD [nm]	PDI ± SD	ζ-potential ± SD [mV]	T_c [°C] ± SD	DOX %EE ± SD
0	NA	NA	121.1±3.0	0.07±0.02	-5.4±1.2	42.50±0.05	95±6%
10	73±2%	1.8±0.04	153.9±5.5	0.11±0.03	-8.1±1.0	42.30±0.05	94±2%
20	67.9±1%	3.4±0.03	155.6±4.6	0.11±0.02	-7.6±0.2	42.30±0.05	93±5%
30	62.3±6%	4.7±0.28	138.2±7.4	0.11±0.03	-5.2±0.5	42.30±0.05	91±3%
50	58±10%	7.3±0.73	157.3±12.2	0.13±0.03	-7.6±1.5	42.31±0.01	78±8%
Anti-PD1-LTSL	NA	NA	156.9±5.4	0.17±0.10	-8.1±1.8	NA	NA

a) NA: not applicable.

b) SD represents the standard deviation from the average value obtained from three independent experiments.

Table 2. mLTSL as a promising MRI T_2 contrast agent. Calculated longitudinal r_1 and transverse r_2 relaxivities for HCA-coated IO NPs and mLTSL (NPs-to-lipid ratios 30 g/mol) with corresponding r_2/r_1 ratios.

Sample	r_1 [$s^{-1} \text{ mM}^{-1}$]	r_2 [$s^{-1} \text{ mM}^{-1}$]	r_2 / r_1
HCA-coated IO NPs	0.85 ± 0.04	3.2 ± 0.8	3.8
mLTSL	0.29 ± 0.02	333 ± 13	1148